CHAPTER

Radiation and scattering of sound by the boundary value method 12

CHAPTER OUTLINE

In this chapter and the next, we will derive results that were used in previous chapters in order to study transducers and their radiation characteristics. The aim is to provide insight into how the shape of a transducer determines its behavior as well as an understanding of how to solve acoustical problems analytically. In each problem a new concept or method is introduced so that each problem is slightly more complicated than the previous one. Formulas are given which the interested reader may use as part of his or her own simulations. In this chapter, we will take the wave equation solutions of Chapter 2 and apply the appropriate boundary conditions to them in order to determine the unknown coefficients. This is known as the boundary value method. In fact we have already used this method to solve for the reflection of a plane wave from a plane in Sec. 4.9, radiation from a pulsating sphere in Sec. 4.10, and an oscillating sphere Sec. 4.15. In Chapter 13, we will treat sound sources as arrays of point sources which are integrated using the boundary integral method.

PART XXXIII: RADIATION IN CYLINDRICAL COORDINATES

12.1 RADIATION FROM A PULSATING INFINITE CYLINDER

The infinitely long pulsating cylinder is a useful model for vertical loudspeaker arrays. If the height of the array is much greater than the wavelength of the sound being radiated, then we can use a two-

Acoustics: Sound Fields and Transducers. DOI: 10.1016/B978-0-12-391421-7.00012-9

dimensional model of infinite extent. Due to axial symmetry, it can be treated as a one-dimensional problem with just a single radial ordinate w.

Pressure field. Since the cylinder is radiating into free space, where there are no reflections, we take the outward-going part of the solution to the cylindrical wave equation (2.90) given by Eq. (2.94), where $\tilde{p}_+$ is an unknown coefficient to be determined from the boundary conditions. Let us now impose a boundary condition at the surface of the cylinder whereby the particle velocity normal to the surface, given by Eq. (2.95), is equal to the uniform surface velocity $\tilde{u}_0$ so that $\tilde{u}(a) = \tilde{u}_0$, where a is the radius, which gives

$$\tilde{p}_+ = \frac{j\rho_0 c\tilde{u}_0}{H_1^{(2)}(ka)}. \tag{12.1}$$

Inserting this into Eq. (2.94) and substituting $\tilde{U}_0/l = 2\pi a\tilde{u}_0$, where $\tilde{U}_0/l$ is the total volume velocity per unit length, yields

$$\tilde{p}(w) = \frac{j\rho_0 c(\tilde{U}_0/l)}{2\pi a H_1^{(2)}(ka)} H_0^{(2)}(kw). \tag{12.2}$$

12.2 RADIATION FROM AN INFINITE LINE SOURCE

In the limit as the radius of the cylinder shrinks to zero, we have an infinite line source. In Sec. 13.14 we will use this as a building block for an infinite ribbon which can be treated as an array of line sources using the Huygens–Fresnel principle. When the radius is very small, we find that

$$H_1^{(2)}(ka)|_{a\to 0} = \frac{2j}{\pi ka}, \tag{12.3}$$

which after inserting into Eq. (12.2) gives the pressure field of an infinite line source:

$$\tilde{p}(w) = \frac{k\rho_0 c(\tilde{U}_0/l)}{4} H_1^{(2)}(kw). \tag{12.4}$$

In the far field, we find that

$$H_1^{(2)}(kw)|_{w\to\infty} = \sqrt{\frac{2}{\pi kw}} e^{-j(kw-\frac{\pi}{4})}, \tag{12.5}$$

so that the far-field pressure for a line source is given by

$$\tilde{p}(w) = \frac{\rho_0 c(\tilde{U}_0/l)}{2}\sqrt{\frac{k}{2\pi w}} e^{-j(kw-\frac{\pi}{4})}. \tag{12.6}$$

Interestingly, the far-field pressure given by Eq. (12.6) varies with the inverse square-root of the radial distance w from the source so that the SPL falls by 3 dB for every doubling of distance, which is a characteristic of cylindrically diverging waves. This is in contrast to a spherically diverging wave,

where the pressure given by Eq. (2.107) varies with the inverse square of the radial distance r from the source so that the SPL falls by 6 dB for every doubling of distance. Hence line sources, in the form of vertical stacks of loudspeakers, are popular in auditoriums because they give a more uniform sound pressure distribution.

PART XXXIV: RADIATION AND SCATTERING IN SPHERICAL COORDINATES

12.3 SCATTERING OF A PLANE WAVE FROM A RIGID SPHERE

In this example, the expression *scattering* has been applied rather than *reflection* because not only does a sphere reflect sound, but sound waves can bend around it, a phenomenon known as *diffraction*. Generally, scattering refers to a mixture of reflection and diffraction. In the case of reflection from a plane (see Sec. 4.9), we used rectangular coordinates in x and y. Here we are considering a sphere [1], so it is convenient to use axially symmetrical spherical coordinates in r and θ as shown in Fig. 12.1. In general, the solution for the *resultant field* is the sum of the *incident field* in the absence of any obstacle and the *scattered field* which is that which would be produced if the obstacle itself were radiating with a notional surface velocity which is normal to its surface. If the object is rigid, this notional velocity must be equal and opposite to the component of velocity of the incident wave that is normal to the surface of the obstacle in its absence. The result of this is to produce zero net velocity normal to the surface of the obstacle when it is present in the resultant field. Because the incident wave front arrives at different parts of the surface at different times, the normal surface velocity varies in magnitude and phase over θ, except when the wavelength is very large compared with the diameter of the sphere, in which case it behaves as a simple omnidirectional source or pulsating sphere as discussed in Sec. 4.10.

Incident field. In spherical coordinates, the incident plane wave pressure is

$$\tilde{p}_I(r,\theta) = \tilde{p}_0 e^{-jkr\cos\theta}. \tag{12.7}$$

Fortunately, this expression can be expanded in terms of spherical Bessel functions j_n and Legendre functions P_n as follows:

$$\tilde{p}_I(r,\theta) = \tilde{p}_0 \sum_{n=0}^{\infty} (-j)^n (2n+1)\, j_n(kr) P_n(\cos\theta). \tag{12.8}$$

This expression, which is similar in form to Eq. (2.164) for the solution to the wave equation in spherical coordinates, is treated more rigorously later in the derivation of Eq. (13.63).

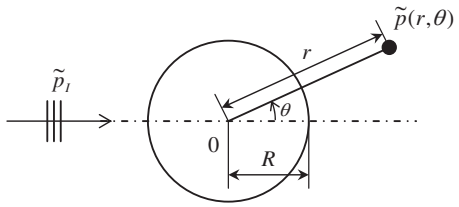

FIG. 12.1 Geometry of plane wave and sphere.

Scattered field. We assume that the pressure field scattered from the sphere is a solution to Eq. (2.145), the Helmholtz wave equation in spherical coordinates. However, due to axial symmetry, we can ignore Eq. (2.162) for the azimuthal part of the solution. Furthermore, since the sphere is in free space, there are no waves reflected back towards the sphere (Sommerfeld condition). Hence we can take just the outward-traveling part of Eq. (2.151) for the radial part of the solution. Combining this with Eq. (2.160) for the inclinational part of the solution gives

$$\tilde{p}_s(r,\theta) = \tilde{p}_0 \sum_{n=0}^{\infty} A_n h_n^{(2)}(kr) P_n(\cos\theta), \tag{12.9}$$

where A_n are unknown series coefficients that are determined by applying appropriate boundary conditions.

Resultant field. Using the principle of *superposition of fields*, we now express the resultant field $\tilde{p}(r,\theta)$ as the sum of the incident and scattered fields:

$$\tilde{p}(r,\theta) = \tilde{p}_I(r,\theta) + \tilde{p}_s(r,\theta). \tag{12.10}$$

At the rigid surface of the sphere, where $r = R$, we have the boundary condition of zero normal velocity. Hence from Eq. (2.4*a*), the pressure gradient must also be zero:

$$\frac{\partial}{\partial r}\,\tilde{p}(r,\theta)\big|_{r=R} = 0, \tag{12.11}$$

so that

$$\frac{\partial}{\partial r}\,\tilde{p}_s(r,\theta)\big|_{r=R} = -\frac{\partial}{\partial r}\,\tilde{p}_I(r,\theta)\,|_{\,r=R}. \tag{12.12}$$

What this equation tells us is that the scattered field is that which would be produced if the surface of the sphere itself were oscillating with a velocity *equal and opposite* to the normal velocity of the incident wave at the surface in the absence of the sphere. Inserting the expressions for $\tilde{p}_s$ and $\tilde{p}_I$ from Eqs. (12.9) and (12.8) respectively into Eq. (12.12) gives

$$\sum_{n=0}^{\infty} A_n h_n'^{(2)}(kR) P_n(\cos\theta) = -\sum_{n=0}^{\infty} (-j)^n (2n+1) j_n'(kR) P_n(\cos\theta), \qquad 0 \le \theta \le \pi, \tag{12.13}$$

where

$$j_n'(kR) = \frac{\partial}{\partial r}\,j_n(kr)\big|_{r=R} = \frac{k}{2n+1}\left(n j_{n-1}(kR) - (n+1) j_{n+1}(kR)\right), \tag{12.14}$$

$$h_n'^{(2)}(kR) = \frac{\partial}{\partial r}\,h_n^{(2)}(kr)\big|_{r=R} = \frac{k}{2n+1}\left(n h_{n-1}^{(2)}(kR) - (n+1) h_{n+1}^{(2)}(kR)\right). \tag{12.15}$$

Straight away, by matching the coefficients of $P_n(\cos\theta)$ on both sides of Eq. (12.13), we can see that the unknown coefficients A_n are given by

$$A_n = -(-j)^n (2n+1)\,\frac{j_n'(kR)}{h_n'^{(2)}(kR)}. \tag{12.16}$$

Inserting Eq. (12.16) into Eq. (12.9) gives the scattered field as

$$\tilde{p}_s(r,\theta) \;=\; -\tilde{p}_0 \sum_{n=0}^{\infty} (-j)^n (2n+1)\, \frac{j_n'(kR)}{h_n'^{(2)}(kr)}\, h_n^{(2)}(kr) P_n(\cos\theta). \tag{12.17}$$

The resultant field $\tilde{p}(r,\theta)$ is then given by Eq. (12.10) using Eq. (12.7) for $\tilde{p}_I(r,\theta)$ and Eq. (12.17) for $\tilde{p}_S(r,\theta)$. The magnitude of the normalized pressure $|\tilde{p}(w,z)/\tilde{p}_0|$ is plotted in Fig. 12.2 and Fig. 12.3 in cylindrical coordinates w and z where $r = \sqrt{w^2+z^2}$ and $\cos\theta = Z/\sqrt{w^2+z^2}$. It can be seen from Fig. 12.2 that the incident field is hardly disturbed at all when $kR = 0.1$, i.e., when the wavelength is much greater than the circumference of the sphere. On the other hand, at the other end of the spectrum, the plot for $kR = 10$ in Fig. 12.3 tells us that there are significant interference patterns in the vicinity of the sphere when the wavelength is considerably shorter than the circumference of the sphere.

Far-field pressure. As the distance r from the centre of the sphere is increased to many wavelengths, the asymptotic expression for the spherical Hankel function becomes

$$h_n^{(2)}(kr)|_{r\to\infty} \;= \frac{j^{n+1}}{kr}\, e^{-jkr}. \tag{12.18}$$

Inserting this into Eq. (12.17) yields

$$\tilde{p}_s(r,\theta)|_{r\to\infty} \;=\; -\frac{jR\,\tilde{p}_0}{2r}\, e^{-jkr}\, D(\theta), \tag{12.19}$$

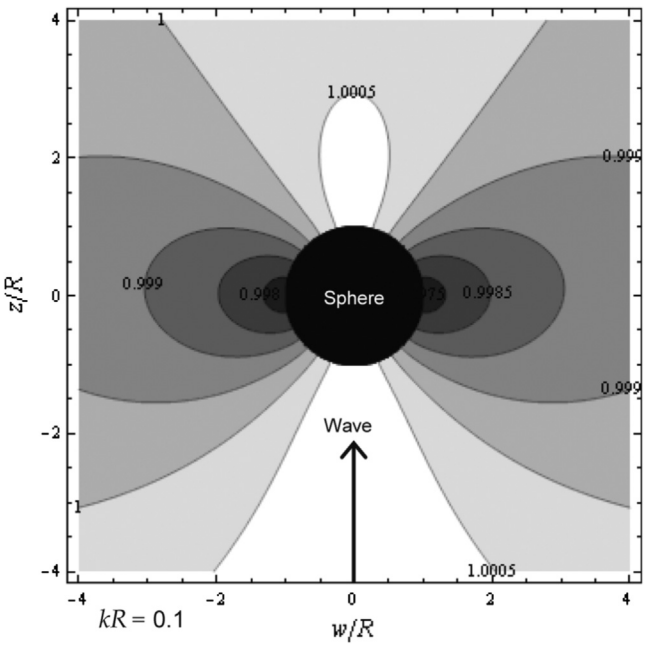

FIG. 12.2 Resultant pressure field $|\tilde{p}(w,z)/\tilde{p}_0|$ due to the scattering of a plane wave from a sphere for $kR = 0.1$.

The arrow shows the direction of the incident wave.

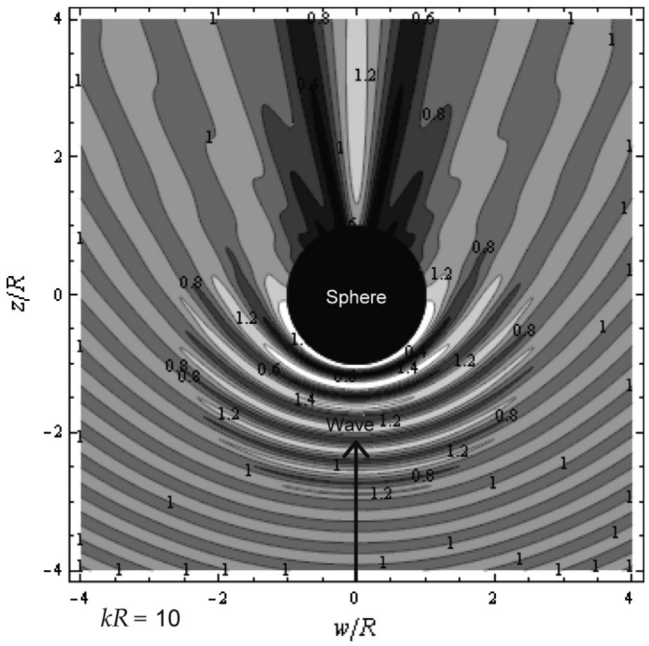

FIG. 12.3 Resultant pressure field $|\tilde{p}(w,z)/\tilde{p}_0|$ due to the scattering of a plane wave from a sphere for $kR = 10$.

The arrow shows the direction of the incident wave.

where $D(\theta)$ is a directivity function given by

$$D(\theta) = \frac{2}{kR}\sum_{n=0}^{\infty}(2n+1)\frac{j_n'(kR)}{h_n'^{(2)}(kR)}P_n(\cos\theta). \tag{12.20}$$

The directivity pattern $20\log_{10}(D(\theta)/D(0))$ is plotted in Fig. 12.4 for various values of kR.
Let a reflection coefficient be defined by

$$D(\pi) = \frac{2}{kR}\sum_{n=0}^{\infty}(-1)^n(2n+1)\frac{j_n'(kR)}{h_n'^{(2)}(kR)} \approx \begin{cases} -5jk^2R^2/3, & kR < 0.5 \\ -1, & kR > 2, \end{cases} \tag{12.21}$$

where we have used the identity $P_n(-1) = (-1)^n$. Similarly, let a transmission coefficient be defined by

$$D(0) = \frac{2}{kR}\sum_{n=0}^{\infty}(2n+1)\frac{j_n'(kR)}{h_n'^{(2)}(kR)} \approx \begin{cases} jk^2R^2/3, & kR < 0.5 \\ kR, & kR > 10, \end{cases} \tag{12.22}$$

where we have used the identity $P_n(1) = 1$. These reflection and transmission coefficients are plotted against kR in Fig. 12.5.

For small values of kR, the transmission and reflection coefficients are both fairly weak. We see that, above $kR = 2$, the reflection coefficient remains virtually constant whereas the transmission

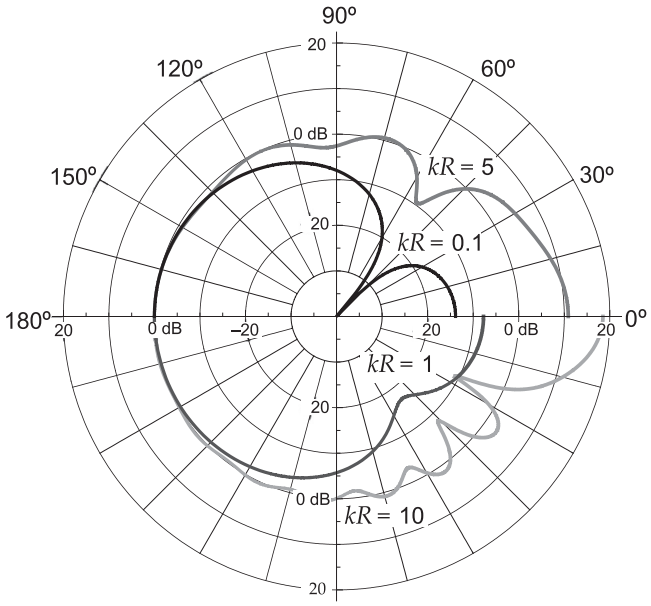

FIG. 12.4 Directivity pattern 20 $\log_{10}(|D(\theta)|/|D(\pi)|)$ of the far-field pressure due to the scattering of a plane wave from a rigid sphere (excluding the incident field).

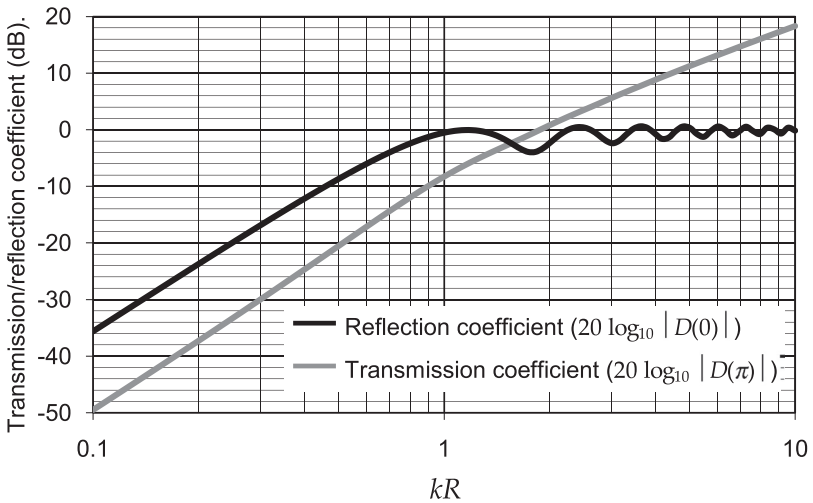

FIG. 12.5 Transmission and reflection coefficients for the scattering of a plane wave by a rigid sphere.

coefficient shows that energy is concentrated in the direction of the incident wave. This can also be seen from Fig. 12.3. This may seem somewhat counter-intuitive since one might expect an obstacle to cast a shadow at high frequencies and we will see later that this is indeed the case when the obstacle is planar. However, in this case the smooth continuous contours or the sphere enable sound waves to be diffracted around it at high frequencies. The fact that higher frequency waves are scattered more than lower frequency ones is also true for light, which explains why the sky is blue.

12.4 SCATTERING FROM A RIGID SPHERE BY A POINT SOURCE

Refer to Fig. 12.6. Let a point source of volume velocity $\tilde{U}_0$ be located at a distance d from a sphere of radius R. We wish to calculate the resultant pressure field $\tilde{p}(r, \theta)$ at a distance r from the center of the sphere and at an angle θ with the axis passing through the point source and center of the sphere. The distance r_1 between the observation point and the point source is given by

$$r_1 = \sqrt{r^2 + d^2 - 2rd\cos\theta}. \tag{12.23}$$

Incident field. In spherical coordinates, the incident pressure field due to the point source is obtained by substituting $r = r_1$ in Eq. (4.71) to give

$$\tilde{p}_I(r, \theta) = -jk\rho_0 c\tilde{U}_0 \frac{e^{-jkr_1}}{4\pi r_1}. \tag{12.24}$$

This expression can be expanded in terms of spherical Bessel functions j_n and Legendre functions P_n from Eq. (13.68) as follows

$$\tilde{p}_I(r, \theta) = -\frac{k^2\rho_0 c\tilde{U}_0}{4\pi}\sum_{n=0}^{\infty}(2n+1)h_n^{(2)}(kd)j_n(kr)P_n(\cos\theta), \qquad r \le d. \tag{12.25}$$

Scattered field. As in the case of the previous problem of the plane wave and a sphere, we assume that the pressure field scattered from the sphere is a general axisymmetric solution to Eq. (2.145), the Helmholtz wave equation in spherical coordinates:

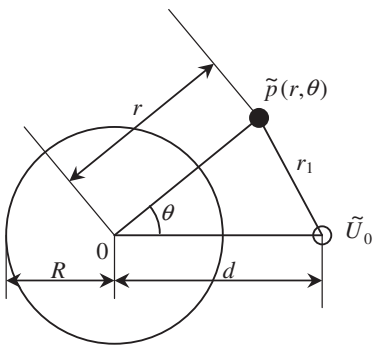

FIG. 12.6 Geometry of point source and sphere.

$$\tilde{p}_s(r,\theta) = \frac{\rho_0 c \tilde{U}_0}{4\pi R^2} \sum_{n=0}^{\infty} A_n h_n^{(2)}(kr) P_n(\cos\theta), \tag{12.26}$$

where A_n are unknown series coefficients that are determined by applying appropriate boundary conditions. However, this time the solution is in terms of the source volume velocity instead of pressure. In order to keep the coefficients A_n dimensionless, the volume velocity has been converted into a particle velocity by dividing it by the surface area of the sphere $S = 4\pi R^2$ and then converted to a pressure term by multiplying it by the specific acoustic impedance of free space $\rho_0 c$.

Resultant field. Using the principle of *superposition of fields*, we now express the resultant field $\tilde{p}(r,\theta)$ as the sum of the incident and scattered fields:

$$\tilde{p}(r,\theta) = \tilde{p}_I(r,\theta) + \tilde{p}_s(r,\theta). \tag{12.27}$$

At the rigid surface of the sphere, where $r = R$, we have the boundary condition of zero normal velocity. Hence from Eq. (2.4*a*), the pressure gradient must also be zero:

$$\frac{\partial}{\partial r}\tilde{p}(r,\theta)|_{r=R} = 0, \tag{12.28}$$

so that

$$\frac{\partial}{\partial r}\tilde{p}_s(r,\theta)|_{r=R} = -\frac{\partial}{\partial r}\tilde{p}_I(r,\theta)|_{r=R}, \tag{12.29}$$

which, after inserting the expressions for $\tilde{p}_s$ and $\tilde{p}_I$ from Eqs. (12.26) and (12.25) respectively gives

$$\sum_{n=0}^{\infty} A_n h_n'^{(2)}(kR) P_n(\cos\theta) = k^2 R^2 \sum_{n=0}^{\infty} (2n+1) h_n^{(2)}(kd) j_n'(kR)\, P_n(\cos\theta), \quad 0 \le \theta \le \pi, \tag{12.30}$$

where

$$j_n'(kR) = \frac{\partial}{\partial r} j_n(kr)|_{r=R} = \frac{k}{2n+1}\left(n j_{n-1}(kR) - (n+1) j_{n+1}(kR)\right), \tag{12.31}$$

$$h_n'^{(2)}(kR) = \frac{\partial}{\partial r} h_n^{(2)}(kr)|_{r=R} = \frac{k}{2n+1}\left(n h_{n-1}^{(2)}(kR) - (n+1) h_{n+1}^{(2)}(kR)\right). \tag{12.32}$$

Straight away, by matching the coefficients of $P_n(\cos\theta)$ on both sides of Eq. (12.30), we can see that the unknown coefficients A_n are given by

$$A_n = k^2 R^2 (2n+1) h_n^{(2)}(kd) \frac{j_n'(kR)}{h_n'^{(2)}(kR)}. \tag{12.33}$$

Inserting Eq. (12.33) into Eq. (12.26) gives the scattered field as

$$\tilde{p}_s(r,\theta) = k^2 R^2 \frac{\rho_0 c \tilde{U}_0}{S} \sum_{n=0}^{\infty} (2n+1) h_n^{(2)}(kd) \frac{j_n'(kR)}{h_n'^{(2)}(kR)}\, h_n^{(2)}(kr) P_n(\cos\theta), \tag{12.34}$$

where $S = 4\pi R^2$ is the total surface area of the sphere. The resultant field $\tilde{p}(r, \theta)$ is then given by Eq. (12.27) using Eq. (12.24) for $\tilde{p}_I(r, \theta)$ and Eq. (12.34) for $\tilde{p}_S(r, \theta)$. The magnitude of the normalized pressure,

$$\left| S\tilde{p}(w, z)/(\rho c \tilde{U}_0) \right|,$$

is plotted in Fig. 12.7 and Fig. 12.8 in cylindrical coordinates w and z where

$$r = \sqrt{w^2 + z^2} \quad \text{and} \quad \cos\theta = z/\sqrt{w^2 + z^2}.$$

It can be seen from Fig. 12.7 that the incident field is hardly disturbed at all when $kR = 0.1$, i.e., when the wavelength is much greater than the circumference of the sphere, except that the constant pressure contours are distorted slightly so that they become normal to the surface of the sphere. On the other hand, at the other end of the spectrum, the plot for $kR = 10$ in Fig. 12.3 tells us that there are significant interference patterns in the vicinity of the sphere when the wavelength is considerably shorter than the circumference of the sphere. Also, the shadow regions are more distinct than those that are produced by an incident plane wave in Fig. 12.3.

Far-field pressure. As the distance r from the centre of the sphere is increased to many wavelengths, the asymptotic expression for the spherical Hankel function becomes that of Eq. (12.18). Inserting Eq. (12.18) into Eq. (12.34) yields

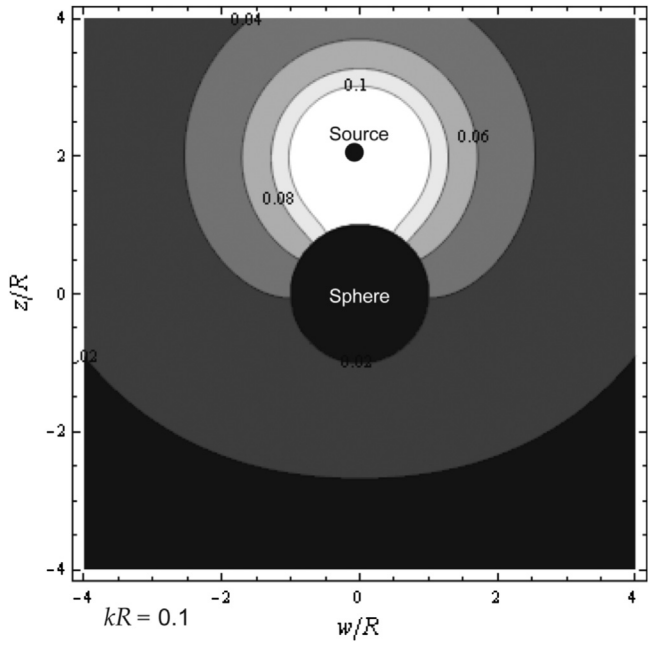

FIG. 12.7 Resultant pressure $|S\,\tilde{p}(w, z)/\rho c\tilde{U}_0|$ field due to the scattering of a point source from a rigid sphere for $kR = 0.1$.

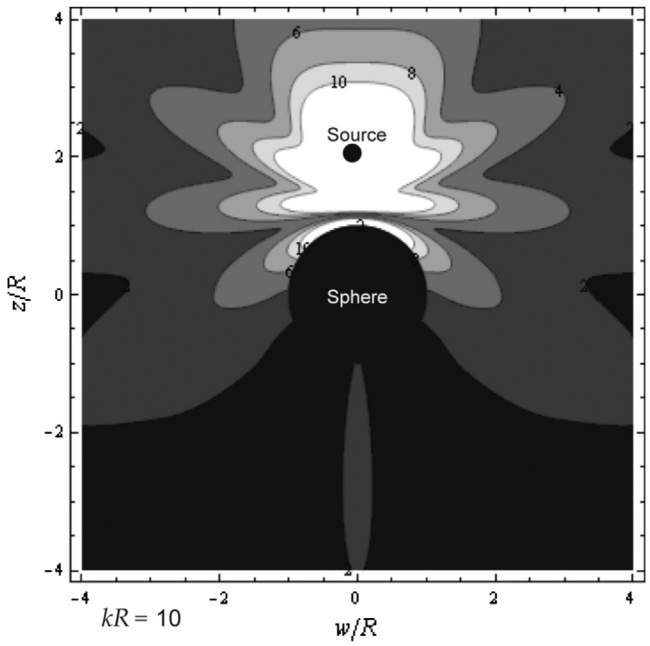

FIG. 12.8 Resultant pressure field $|S\,\tilde{p}(w,z)/\rho c\tilde{U}_0|$ due to the scattering of a field from a point source by a rigid sphere where $kR = 10$.

$$\tilde{p}_s(r,\theta)|_{r\to\infty} = -\frac{jk\rho_0 c\tilde{U}_0}{4\pi r}\, e^{-jkr}\, D(\theta), \tag{12.35}$$

where $D(\theta)$ is a directivity function given by

$$D(\theta) = -\sum_{n=0}^{\infty} j^n(2n+1)h_n^{(2)}(kd)\frac{j_n'(kR)}{h_n'^{(2)}(kR)}P_n(\cos\theta). \tag{12.36}$$

The directivity pattern $20\log_{10}(D(\theta)/D(0))$ is plotted in Fig. 12.9 for various values of kR. Let a reflection coefficient be defined by

$$D(0) = -\sum_{n=0}^{\infty} j^n(2n+1)h_n^{(2)}(kd)\frac{j_n'(kR)}{h_n'^{(2)}(kR)}, \tag{12.37}$$

where we have used the identity $P_n(1) = 1$. Similarly, let a transmission coefficient be defined by

$$D(\pi) = -\sum_{n=0}^{\infty} (-j^n)(2n+1)h_n^{(2)}(kd)\frac{j_n'(kR)}{h_n'^{(2)}(kR)}, \tag{12.38}$$

where we have used the identity $P_n(-1) = (-1)^n$. These reflection and transmission coefficients are plotted against kR in Fig. 12.10 and Fig. 12.11. For small values of kR, the transmission and reflection

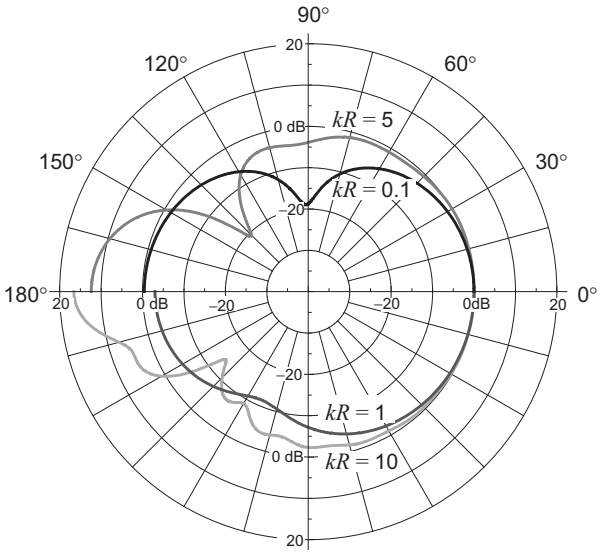

FIG. 12.9 Directivity pattern 20 $\log_{10}(|D(\theta)|/|D(0)|)$ of the far-field pressure for $d = 2R$ due to the scattering of a point source from a rigid sphere (excluding the incident field).

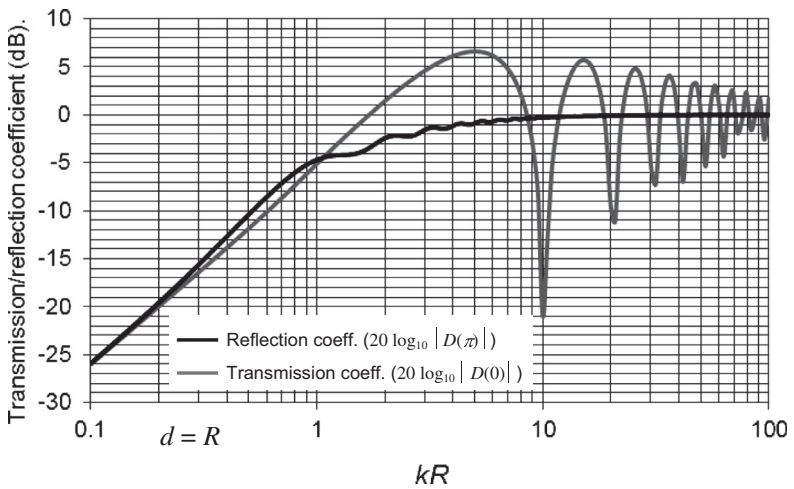

FIG. 12.10 Transmission and reflection coefficients for the scattering of a point source by a rigid sphere for $d = R$.

Frequency is plotted on a normalized scale, where $kR = 2\pi R/\lambda = 2\pi fR/c$.

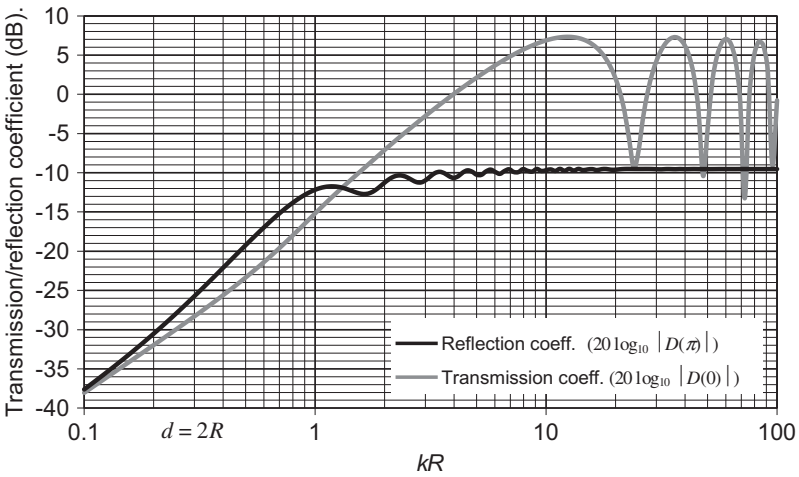

FIG. 12.11 Transmission and reflection coefficients for the scattering of a point source by a rigid sphere for $d = 2R$.

Frequency is plotted on a normalized scale, where $kR = 2\pi R/\lambda = 2\pi fR/c$.

coefficients are both fairly weak, but more or less equal because the sound is scattered in all directions. It can be seen that above $kR = 2$, the reflection coefficient remains virtually constant. In the plot for $d = R$, the point source is on the surface of the sphere and the reflection coefficient above $kR = 2$ is 100% because the point source is behaving as though it is on an infinite plane. In the plot for $d = 2R$, the reflected wave has decayed over twice the distance between the point source and the sphere. We will study the behavior of a point source on a sphere in greater detail when dealing with sound sources. Above $kR = 10$, we do not see the rising transmission coefficient that we saw with the plane wave. Instead, it oscillates around unity (0 dB) due to constructive and destructive interference. Hence, the sound from a point source is not concentrated by the sphere like that from a plane wave. The reason for this is that components of the plane wave strike the sphere from many different directions, including the sides, and these components can be diffracted around it.

12.5 RADIATION FROM A POINT SOURCE ON A SPHERE

This problem is essentially the same as the last one when $d = R$. However, this time we shall introduce the property of orthogonality in order to obtain a simple solution. By *reciprocity*, the resulting expression can be used to obtain the pressure at a point on the sphere due to a source at some point in space. This is a useful model for the diffraction effects of the human head on sound arriving at one ear, assuming a hard sphere model of the head. Unlike the pulsating sphere, only an infinitesimally small part of the surface is oscillating, so that the velocity distribution is described by

$$\tilde{u}(R,\theta) = \begin{cases} \tilde{u}_0, & 0 \le \theta \le \delta \\ 0, & \delta \le \theta \le \pi \end{cases}, \tag{12.39}$$

where δ is a vanishingly small angle.

Near-field pressure. We assume that the pressure field generated is a general axisymmetric solution to Eq. (2.145), the Helmholtz wave equation in spherical coordinates:

$$\tilde{p}(r,\theta) \;=\; \rho_0 c\tilde{u}_0 \sum_{n=0}^{\infty} A_n h_n^{(2)}(kr)\, P_n(\cos\,\theta). \tag{12.40}$$

Applying the velocity boundary condition gives

$$\begin{aligned}\tilde{u}(R,\theta) \;&=\; \frac{1}{-jk\rho_0 c}\;\frac{\partial}{\partial r}\,p(r,\theta)|_{\,r=R} \\ &=\; \frac{\tilde{u}_0}{-jk}\sum_{n=0}^{\infty} A_n h'^{(2)}_n(kR) P_n(\cos\,\theta) \;=\; \begin{cases} \tilde{u}_0, & 0 \le \theta \le \delta \\ 0, & \delta \le \theta \le \pi, \end{cases}\end{aligned} \tag{12.41}$$

where the derivative of the spherical Hankel function $h_n'^{(2)}(kR)$ is given by Eq. (12.32). We now multiply both sides of (12.41) with the orthogonal function $P_m\,(\cos\,\theta)$ and integrate over the surface of the sphere, where the area of each surface element is given by

$$\delta S \;=\; 2\pi R^2\,\sin\,\theta\;\delta\theta,$$

so that

$$\frac{1}{-jk}\sum_{n=0}^{\infty} A_n h'^{(2)}_n(kR)\int_0^{\pi} P_n(\cos\,\theta)\,P_m(\cos\,\theta)\,R\sin\,\theta\,d\theta \;=\; \int_0^{\delta} P_m(\cos\,\theta)\,R\sin\,\theta\,d\theta \tag{12.42}$$

It can be seen from Eq. (12.42) that we have effectively exchanged θ dependency for m dependency. Hence Eq. (12.42) represents an infinite set of simultaneous equations where $m = 0,\,1,\,2,\,\cdots$. The integral solutions are given by Eqs. (66) and (67) in Appendix II. However, δ_{mn} is the Kronecker delta function which is zero unless $m = n$ in which case its value is 1. In other words, we have a matrix in which only the diagonal terms are non-zero, so that the coefficients are given directly by

$$A_n \;=\; -jk\frac{(2n+1)\,\delta^2}{4h'^{(2)}_n(kR)} \tag{12.43}$$

without having to solve a system of equations. Finally, by inserting (12.43) in (12.40) and letting $\tilde{U}_0 \;=\; \pi(\delta R)^2\tilde{u}_0$ we can write the near-field pressure as

$$\tilde{p}(r,\theta) \;=\; -j\rho_0 c\frac{\tilde{U}_0}{S}\sum_{n=0}^{\infty}\frac{(2n+1)^2 h_n^{(2)}(kr)P_n(\cos\,\theta)}{nh_{n-1}^{(2)}(kR) - (n+1)h_{n+1}^{(2)}(kR)}, \tag{12.44}$$

where $S = 4\pi R^2$ is the total surface area of the sphere. The magnitude of the normalized pressure,

$$\left|S\,\tilde{p}(w,z)/(\rho_0 c\tilde{U}_0)\right|,$$

is plotted in Fig. 12.12 and Fig. 12.13 in cylindrical coordinates w and z where

$$r = \sqrt{w^2 + z^2} \quad \text{and} \quad \cos\theta = z/\sqrt{w^2 + z^2}.$$

We can see from Fig. 12.12 that at low frequencies the pressure contours are more or less concentric with the acoustic center at a distance of around ½R in front of the point source. By contrast, the contours in Fig. 12.13 are eccentric so that at high frequencies, the further you are from the source, the further the source appears to be from its actual position.

Far-field pressure. In the far field, we can use the asymptotic expression for the spherical Hankel function from Eq. (12.18), which when inserted into Eq. (12.44) gives

$$\tilde{p}(r,\theta)|_{r\to\infty} = -jk\rho_0 c \frac{\tilde{U}_0}{4\pi r} e^{-jkr} D(\theta), \tag{12.45}$$

where

$$D(\theta) = \frac{1}{k^2R^2} \sum_{n=0}^{\infty} \frac{j^{n+1}(2n+1)^2 P_n(\cos\theta)}{nh_{n-1}^{(2)}(kR) - (n+1)h_{n+1}^{(2)}(kR)}. \tag{12.46}$$

The directivity pattern $20\log_{10}(D(\theta)/D(0))$ is plotted in Fig. 12.14 for various values of kR. The far-field on-axis response is given by

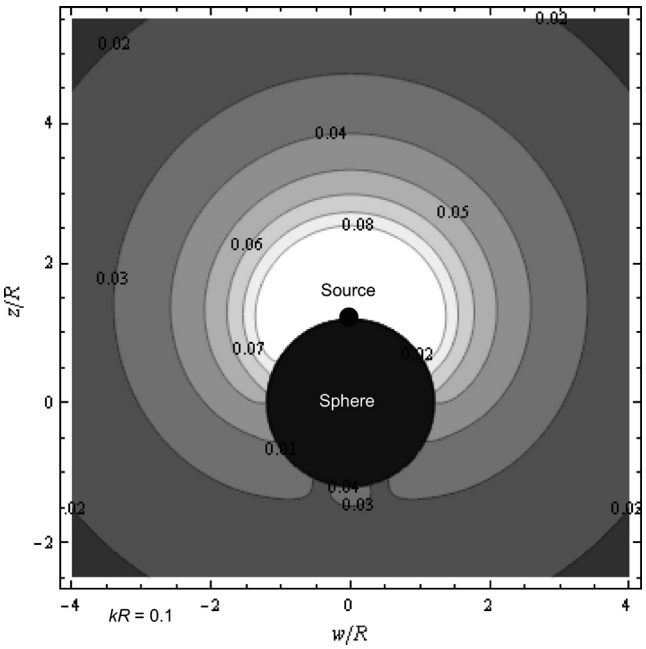

FIG. 12.12 Pressure field $|S\,\tilde{p}(w,z)/\rho_0 c\tilde{U}_0|$ due to a point source on a rigid sphere for $kR = 0.1$.

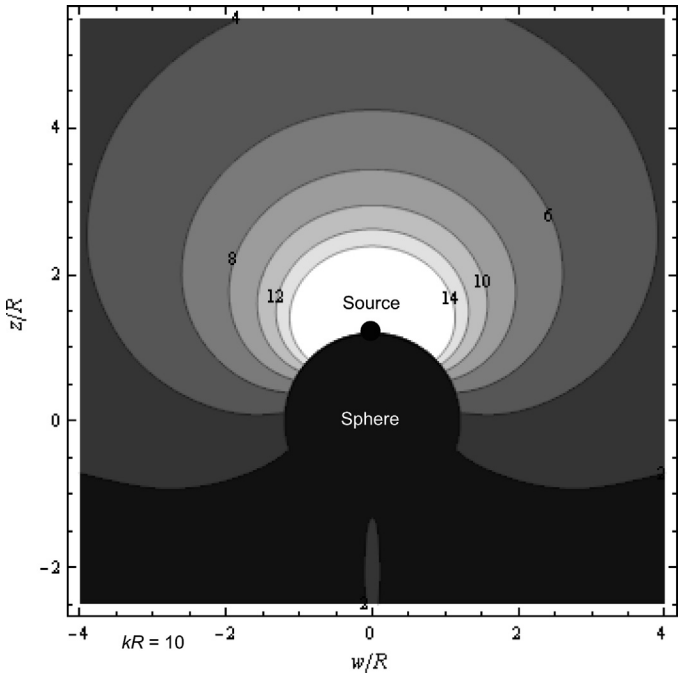

FIG. 12.13 Pressure field $|S\,\tilde{p}(w,z)/\rho_0 c\tilde{U}_0|$ due to a point source on a rigid sphere for $kR = 10$.

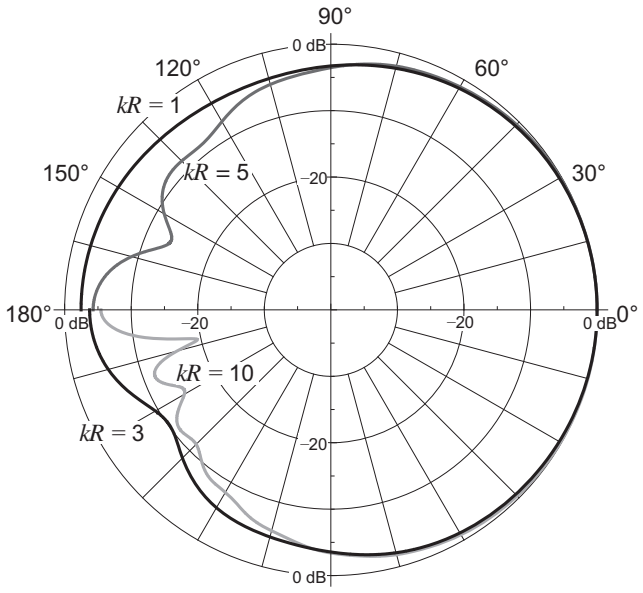

FIG. 12.14 Far field directivity pattern $20\log_{10}(|D(\theta)|/|D(0)|)$ of the far-field pressure due to a point source on a rigid sphere of radius R.

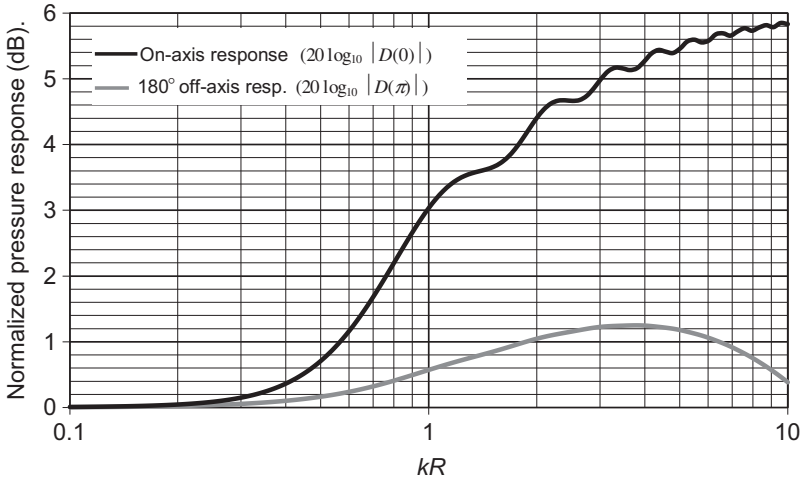

FIG. 12.15 Plots of 20 $\log_{10}(D(0))$ and 20 $\log_{10}(D(\pi))$ where $D(\theta)$ is the directivity function of a point source on a rigid sphere of radius R.

Frequency is plotted on a normalized scale, where $kR = 2\pi R/\lambda = 2\pi fR/c$.

$$D(0) = \frac{1}{k^2R^2}\sum_{n=0}^{\infty}\frac{j^n(2n+1)^2}{nh_{n-1}^{(2)}(kR) - (n+1)h_{n+1}^{(2)}(kR)}. \tag{12.47}$$

The on-axis response 20 $\log_{10}(D(0))$ and 180° off-axis response 20 $\log_{10}(D(\pi))$ are plotted against kR in Fig. 12.15. It can be seen that there is a 6 dB lift in the on-axis response when the wavelength is approximately equal to the circumference of the sphere. This is due to the fact that the point source acts as a pure monopole radiator at low frequencies as though the sphere were not present. However, at high frequencies, the sphere acts as a large baffle and the radiated sound is concentrated in half space thus doubling the pressure value. Because the sphere is smooth and continuous with no reflecting edges, the transition from whole-space to half-space radiation is also smooth, producing just some very small ripples in the on-axis response. We shall see that this is not so in the case of radiators with edges. Hence, the sphere represents an idealized loudspeaker enclosure.

12.6 RADIATION FROM A SPHERICAL CAP IN A SPHERE

In reality, loudspeakers do not have vanishingly small diaphragms and at high frequencies the size and shape of the radiator strongly influences the resulting sound field. The spherical cap [2] represents a curved finite diaphragm which follows the contour of the sphere. This makes it easier to analyze than a flat piston, which we shall consider in the next problem. The spherical cap shown in Fig. 12.16 is set in a rigid sphere of radius R and moves with an axial velocity $\tilde{u}_0$ such that the velocity distribution is described by

$$\tilde{u}(R,\theta) = \begin{cases} \tilde{u}_0\cos\theta, & 0 \le \theta \le \alpha \\ 0, & \alpha \le \theta \le \pi \end{cases}, \tag{12.48}$$

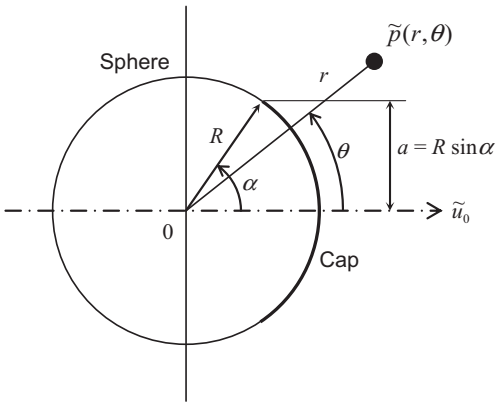

FIG. 12.16 Geometry of oscillating cap in a rigid sphere.

where α is the half-angle of the arc formed by the cap. Although the cap is rigid in this case, other velocity distributions are possible [6]. The total volume velocity is given by

$$\tilde{U}_0 = \tilde{u}_0 R^2 \int_0^{2\pi} \int_0^{\alpha} \cos\theta \sin\theta \, d\theta \, d\phi = S\,\tilde{u}_0, \tag{12.49}$$

where S is the *effective* surface area of the cap given by

$$S = \pi R^2 \sin^2\alpha. \tag{12.50}$$

If the cap were radially pulsating, we would drop the $\cos\theta$ term from Eqs. (12.48) and (12.49) and the effective surface area would be

$$S = 2\pi R^2(1 - \cos\alpha).$$

Near-field pressure. Again we assume that the pressure field generated is a general axisymmetric solution to Eq. (2.145), the Helmholtz wave equation in spherical coordinates:

$$\tilde{p}(r,\theta) = \rho_0 c \tilde{u}_0 \sum_{n=0}^{\infty} A_n h_n^{(2)}(kr)\, P_n(\cos\theta). \tag{12.51}$$

Applying the velocity boundary condition gives

$$\begin{aligned} \tilde{u}(R,\theta) &= \frac{1}{-jk\rho_0 c} \frac{\partial}{\partial r} p(r,\theta)\big|_{r=R} \\ &= \frac{\tilde{u}_0}{-jk} \sum_{n=0}^{\infty} A_n h_n'^{(2)}(kR) P_n(\cos\theta) = \begin{cases} \tilde{u}_0 \cos\theta, & 0 \le \theta \le \alpha \\ 0, & \alpha \le \theta \le \pi, \end{cases} \end{aligned} \tag{12.52}$$

where the derivative of the spherical Hankel function $h_n'^{(2)}(kR)$ is given by Eq. (12.32). We now multiply both sides of Eq. (12.52) with the orthogonal function $P_m(\cos\theta)$ and integrate over the surface of the sphere, where the area of each surface element is given by

$$\delta S = 2\pi R^2 \sin\theta\ \delta\theta,$$

so that

$$\frac{1}{-jk}\sum_{n=0}^{\infty} A_n h_n'^{(2)}(kR)\int_0^{\pi} P_n(\cos\theta)\,P_m(\cos\theta)\ \sin\theta d\theta = \int_0^{\alpha} P_m(\cos\theta)\ \cos\theta\sin\theta\,d\theta \tag{12.53}$$

from which we obtain the coefficients as follows:

$$A_0 = jk\,\frac{-\sin^2\alpha}{4h_0'^{(2)}(kR)}, \tag{12.54}$$

$$A_1 = jk\,\frac{\cos^3\alpha - 1}{2h_1'^{(2)}(kR)}, \tag{12.55}$$

$$A_n = jk(2n+1)\sin\alpha\,\frac{\sin\alpha\,P_n(\cos\alpha) + \cos\alpha\,P_n^1(\cos\alpha)}{2(n-1)(n+2)h_n'^{(2)}(kR)}, \quad n \geq 2, \tag{12.56}$$

where we have used the integral solutions from Eqs. (66) and (68) in Appendix II. Separate terms have been derived for $n=0$ and 1 in Eq. (68) because the expression for $n \geq 2$ is singular at $n=1$. Alternatively, if the cap were radially pulsating, we would drop the $\cos\theta$ term from the right hand side of Eqs. (12.48) and (12.52) and use Eq. (69) from Appendix II. Finally, by inserting Eqs. (12.54), (12.55), and (12.56) in Eq. (12.51) we can write the near-field pressure as

$$\begin{aligned}\tilde{p}(r,\theta) = -jk\rho c\tilde{u}_0\Bigg(&\frac{\sin^2\alpha}{4h_0'^{(2)}(kR)}\,h_0^{(2)}(kr) + \frac{1-\cos^3\alpha}{2h_1'^{(2)}(kR)}\,h_1^{(2)}(kr)\cos\theta \\ &-\sin\alpha\sum_{n=2}^{\infty}(2n+1)\frac{\sin\alpha\,P_n(\cos\alpha)+\cos\alpha\,P_n^1(\cos\alpha)}{2(n-1)(n+2)h_n'^{(2)}(kR)}\,h_n^{(2)}(kr)\,P_n(\cos\theta)\Bigg)\end{aligned} \tag{12.57}$$

Far-field pressure. In the far field, we can use the asymptotic expression for the spherical Hankel function from Eq. (12.18), which when inserted into Eq. (12.57) gives

$$\tilde{p}(r,\theta)|_{r\to\infty} = -jk\rho_0 cS\frac{\tilde{u}_0}{4\pi r}\,e^{-jkr}\,D(\theta), \tag{12.58}$$

where S is the dome effective area given by $S=\pi a^2$ and

$$D(\theta) = -\frac{2}{k^2R^2}\left(\frac{j}{2h_1^{(2)}(kR)} + \frac{3(1-\cos^3\alpha)}{\sin^2\alpha\left(h_0^{(2)}(kR) - 2h_2^{(2)}(kR)\right)}\cos\theta \right. \\ \left. + \sum_{n=2}^{\infty} \frac{j^{n+1}(2n+1)^2\left(\sin\alpha\, P_n(\cos\alpha) + \cos\alpha\, P_n^1(\cos\alpha)\right)}{(n-1)(n+2)\sin\alpha\left(nh_{n-1}^{(2)}(kR) - (n+1)h_{n+1}^{(2)}(kR)\right)} P_n(\cos\theta)\right). \tag{12.59}$$

When $\alpha = ½\pi$, the second term simplifies to that for an oscillating sphere, as described in Sec. 4.15, and odd terms in the expansion vanish so that Eq. (12.59) simplifies to

$$D(\theta)\Big|_{\alpha=\frac{\pi}{2}} = -j\frac{2kRe^{jkR}}{2-k^2R^2+j2kR}\cos\theta \\ -j\frac{2}{k^2R^2}\sum_{n=0}^{\infty}\frac{(-1)^n(4n+1)^2\,P_{2n}(0)}{(2n-1)(2n+1)\left(2nh_{2n-1}^{(2)}(kR) - (2n+1)h_{2n+1}^{(2)}(kR)\right)} P_{2n}(\cos\theta), \tag{12.60}$$

which represents the superposition of two fields. The first term represents an oscillating sphere and the second two diametrically opposed hemispherical caps or a hemispherical dome in an infinite baffle, which will be discussed in greater detail in Sec. 12.9. The same kind of superposition of fields, or "Gutin concept", will be used in Sec. 13.11 to describe a single-sided piston. The directivity pattern 20 $\log_{10}(D(\theta)/D(0))$ for $\alpha = 60°$ is plotted in Fig. 12.17 for various values of ka. As expected, we see that

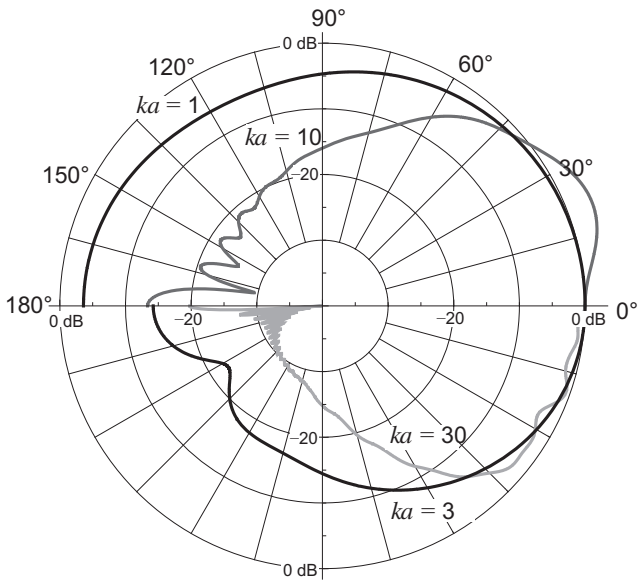

FIG. 12.17 Far-field directivity pattern 20 $\log_{10}(|D(\theta)|/|D(0)|)$ of the far-field pressure due to a spherical cap of radius a in a rigid sphere for $\alpha = 60°$, where α is the half angle of the arc formed by the cap.

at low frequencies the pattern is almost omnidirectional. However, at high frequencies the spherical cap shows a fairly constant angle of dispersion which is approximately equal to the angle of arc formed by the cap itself. The far-field on-axis response is given by

$$D(0) = -\frac{2}{k^2R^2}\left(\frac{j}{2h_1^{(2)}(kR)} + \frac{3(1-\cos^3\alpha)}{\sin^2\alpha\left(h_0^{(2)}(kR) - 2h_2^{(2)}(kR)\right)} + \sum_{n=2}^{\infty}\frac{j^{n+1}(2n+1)^2\left(\sin\alpha\, P_n(\cos\alpha) + \cos\alpha\, P_n^1(\cos\alpha)\right)}{(n-1)(n+2)\sin\alpha\left(nh_{n-1}^{(2)}(kR) - (n+1)h_{n+1}^{(2)}(kR)\right)}\right). \tag{12.61}$$

The on-axis response $20\log_{10}(D(0))$ is plotted against ka in Fig. 12.18. Like the point source on a sphere, we see a rise in the response around $kR = 1$, (i.e. the wavelength is roughly equal to the circumference of the sphere) due to the transition from whole-space to half-space radiation. However, like the oscillating sphere, the response starts to fall above $ka = 5$ because the response is proportional to the cap velocity when the radiation resistance is mainly resistive, as indicated in Fig. 12.19. Unlike the oscillating sphere, the falling response is accompanied by ripples due to the discontinuity at the edge of the cap. This produces cancellation effects due to path length differences from different parts of the cap.

Radiation impedance. The total radiation force $\tilde{F}$ is given by

$$\tilde{F} = R^2\int_0^{2\pi}\int_0^{\alpha}\tilde{p}(R,\theta)\sin\theta\, d\theta\, d\phi \tag{12.62}$$

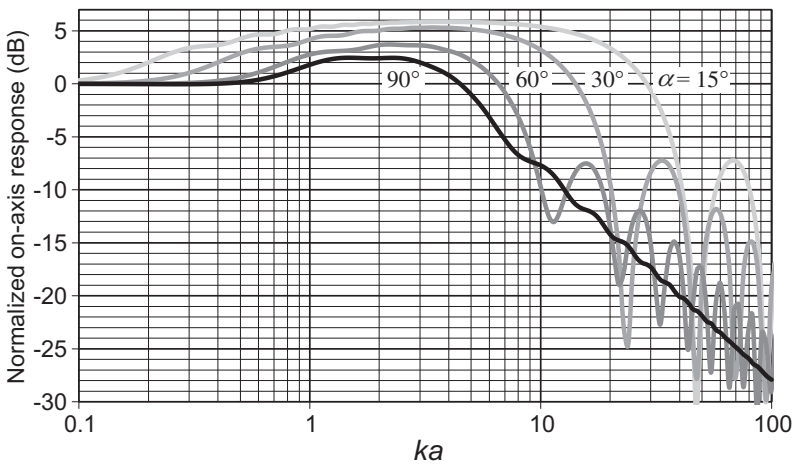

FIG. 12.18 Plot of $20\log_{10}(D(0))$ where $D(\theta)$ is the directivity function of a spherical cap of radius a in a rigid sphere, where α is the half angle of the arc formed by the cap. The axial acceleration of the cap is constant.

Frequency is plotted on a normalized scale, where $ka = 2\pi a/\lambda = 2\pi fa/c$.

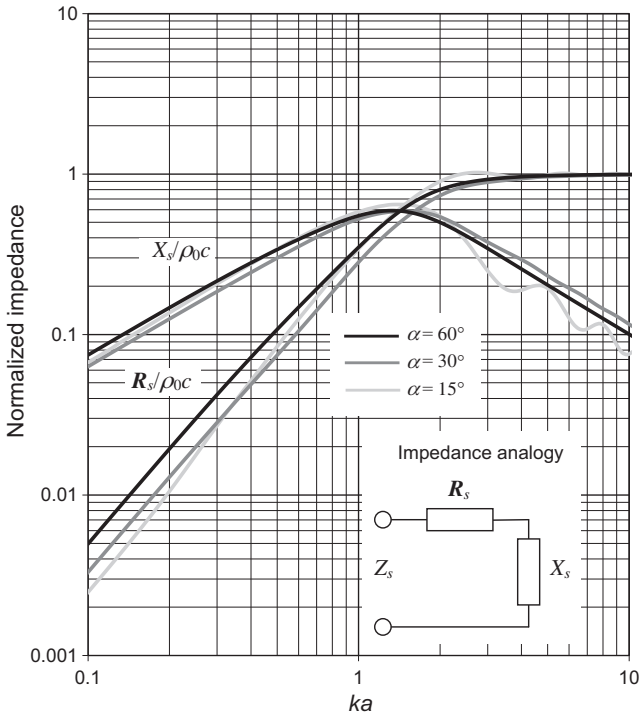

FIG. 12.19 Real and imaginary parts of the normalized specific radiation impedance $Z_s/\rho_0 c$ of the air load on an oscillating spherical cap of radius a in a rigid sphere, where α is the half angle of the arc formed by the cap.

Frequency is plotted on a normalized scale, where $ka = 2\pi a/\lambda = 2\pi fa/c$.

using the identity of Eq. (69) from Appendix II. The specific impedance Z_s is then given by

$$Z_s = \frac{\tilde{F}}{\tilde{U}_0} = \rho_0 c \left(\frac{j(1-\cos\alpha) h_0^{(2)}(kR)}{2h_1^{(2)}(kR)} - \frac{3j(1-\cos^3\alpha) P_1^{-1}(\cos\alpha) h_1^{(2)}(kR)}{\sin\alpha \left(h_0^{(2)}(kR) - 2h_2^{(2)}(kR) \right)} \right.$$
$$\left. + \sum_{n=2}^{\infty} \frac{j(2n+1)^2 \left(\sin\alpha\, P_n(\cos\alpha) + \cos\alpha\, P_n^1(\cos\alpha) \right) P_n^{-1}(\cos\alpha) h_n^{(2)}(kR)}{(n-1)(n+2) \left(nh_{n-1}^{(2)}(kR) - (n+1) h_{n+1}^{(2)}(kR) \right)} \right), \tag{12.63}$$

where we have used the expression for $\tilde{U}_0$ from Eq. (12.49). When $\alpha = \frac{1}{2}\pi$, the second term simplifies to that for an oscillating sphere, as described in Sec. 4.15, and the expansion vanishes so that Eq. (12.63) simplifies to

$$Z_s\big|_{\alpha = \frac{\pi}{2}} = \rho_0 c \left(\frac{k^4R^4 + j(k^3R^3 + 2kR)}{2(k^4R^4 + 4)} + \frac{jh_0^{(2)}(kR)}{2h_1^{(2)}(kR)} \right), \tag{12.64}$$

which represents the superposition of two fields. The first term represents an oscillating sphere and the second two diametrically opposed hemispherical caps or a hemispherical dome in an infinite baffle, which will be discussed in greater detail in Sec. 12.9. The same kind of superposition of fields, or "Gutin concept", will be used in Sec. 13.11 to describe a single-sided piston. The real and imaginary parts, $\boldsymbol{R}_s$ and X_s, are plotted in Fig. 12.19 where

$$Z_s = \boldsymbol{R}_s + jX_s = \Re(Z_s) + j\Im(Z_s). \tag{12.65}$$

We can see that the impedance of the 90° cap is roughly the average of the pulsating and oscillating spheres. At 15°, the cap approaches a piston in an infinite baffle, which we will study later. There are ripples in the impedance curves above $ka = 2$ due to interference patterns in the immediate vicinity of the radiator.

12.7 RADIATION FROM A RECTANGULAR CAP IN A SPHERE

A useful model for the mouth of a circular horn is the spherical cap in a sphere [3]. However, this can be shown to have a somewhat irregular on-axis response with peaks and dips due to interference between sound radiated from the center of the cap and its rim. Also, circular horns are rarely used these days and it is more common to find a rectangular horn with an aspect ratio chosen so that its horizontal radiation is concentrated over an angle which covers the auditorium area. However, one additional advantage of this arrangement is that on-axis irregularities are less likely. The question we wish to answer is what is the optimum aspect ratio for a smooth on-axis response? Until now we have only dealt with problems with axial symmetry, which are independent of the azimuthal angle ϕ. In other words, they are really 2-dimensional in r and θ. The rectangular cap in a sphere is our first genuinely 3-dimensional problem in spherical coordinates (r, θ, ϕ) and its geometry is shown in Fig. 12.20. The rectangular cap, which is defined by the half angles α and β, is set in a rigid sphere of radius R and pulsates with a velocity $\tilde{u}_0$ such that the velocity distribution is described by

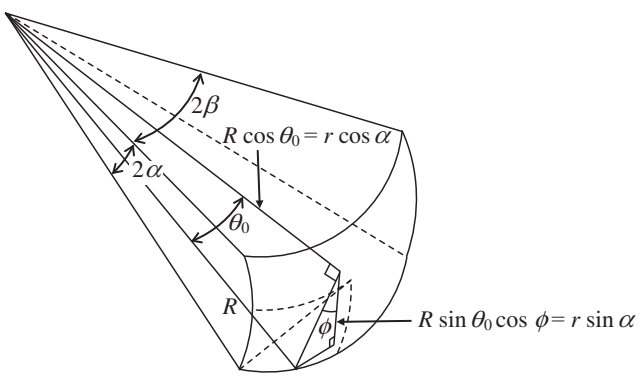

FIG. 12.20 Geometry of rectangular cap in sphere. For clarity the sphere is not shown.

$$\tilde{u}(R,\theta,\phi) = \begin{cases} \tilde{u}_0, & \begin{cases} 0 \le \theta \le \theta_0, & 0 \le \phi \le \arctan\left(\tan\beta/\tan\alpha\right) \\ 0 \le \theta \le \theta_1, & 0 \le \phi \le \arctan\left(\tan\alpha/\tan\beta\right) \end{cases} \\ 0, & \begin{cases} \theta_0 \le \theta \le \pi, & 0 \le \phi \le \arctan\left(\tan\beta/\tan\alpha\right) \\ \theta_1 \le \theta \le \pi, & 0 \le \phi \le \arctan\left(\tan\alpha/\tan\beta\right), \end{cases} \end{cases} \tag{12.66}$$

where

$$\theta_0 = \arctan(\tan\alpha/\cos\phi), \tag{12.67}$$

$$\theta_1 = \arctan(\tan\beta/\cos\phi). \tag{12.68}$$

In order to calculate the *effective* surface area S of the cap, where the area of each surface element is given by

$$\delta S = R^2 \sin\theta\ \delta\theta\ \delta\phi,$$

we need only integrate over one quarter of the cap and multiply the result by four:

$$\begin{aligned} S &= 4R^2 \left(\int_0^{\arctan\frac{\tan\beta}{\tan\alpha}} \int_0^{\arctan\frac{\tan\alpha}{\cos\phi}} \sin\theta\, d\theta\, d\phi + \int_0^{\arctan\frac{\tan\alpha}{\tan\beta}} \int_0^{\arctan\frac{\tan\beta}{\cos\phi}} \sin\theta\, d\theta\, d\phi \right) \\ &= 4R^2 \left\{ \arctan\left(\frac{\tan\alpha\tan\beta}{\sec^2\alpha + \sqrt{\sec^2\alpha + \tan^2\beta}} \right) + \arctan\left(\frac{\tan\alpha\tan\beta}{\sec^2\beta + \sqrt{\sec^2\beta + \tan^2\alpha}} \right) \right\} \\ &\approx 4R^2 \sin\alpha \sin\beta, \qquad \alpha < \frac{\pi}{4}, \qquad \beta < \frac{\pi}{4} \end{aligned} \tag{12.69}$$

Near-field pressure. The Helmholtz wave equation in spherical coordinates is given by

$$\nabla^2 = \frac{\partial^2}{\partial r^2} + \frac{2}{r}\frac{\partial}{\partial r} + \frac{1}{r^2}\frac{\partial^2}{\partial\theta^2} + \frac{1}{r^2\tan\theta}\frac{\partial}{\partial\theta} + \frac{1}{r^2\sin^2\theta}\frac{\partial^2}{\partial\phi^2}, \tag{12.70}$$

The resulting pressure field is given by the following solution:

$$\tilde{p}(r,\theta,\phi) = \rho_0 c\tilde{u}_0 \sum_{n=0}^{\infty} \sum_{m=0}^{n/2} A_{mn} h_n^{(2)}(kr) P_n^{2m}(\cos\theta) \cos 2m\phi. \tag{12.71}$$

where A_{mn} are the as-yet unknown power series coefficients which are evaluated by applying appropriate boundary conditions. In order to meet the boundary condition of symmetry at $\phi = 0$, we use only cosine terms in the solution. Applying the velocity boundary condition gives

$$\begin{aligned} \tilde{u}(R,\theta,\phi) &= \frac{1}{-jk\rho_0 c}\,\frac{\partial}{\partial r}\,p(r,\theta,\phi)|_{\,r=R} \\ &= \frac{\tilde{u}_0}{-jk}\sum_{n=0}^{\infty}\sum_{m=0}^{n/2} A_{mn}h_n'^{(2)}(kR)P_n^{2m}(\cos\theta)\cos 2\,m\phi \end{aligned} \tag{12.72}$$

where the derivative of the spherical Hankel function $h_n'^{(2)}(kR)$ is given by

$$h_n'^{(2)}(kR) = \frac{\partial}{\partial r}\,h_n^{(2)}(kr)\,|_{\,r=R} = \frac{k}{2n+1}\left(nh_{n-1}^{(2)}(kR) - (n+1)h_{n+1}^{(2)}(kR)\right). \tag{12.73}$$

We now equate Eq. (12.66) with Eq. (12.72) while truncating the infinite series limit to N. Then multiplying both sides with the orthogonal function

$$P_q^{2p}(\cos\theta)\cos 2\,p\phi$$

and integrating over the surface of the sphere gives

$$\begin{aligned} &\frac{1}{-jk}\sum_{n=0}^{N}\sum_{m=0}^{n/2} A_{mn}h_n'^{(2)}\,(kR)\int_0^{\pi} P_n^{2m}(\cos\theta)\,P_q^{2p}\,(\cos\theta)\sin\theta\,d\theta\int_0^{2\pi}\cos 2m\,\phi\cos 2\,p\phi\,d\phi \\ &= \int_0^{\arctan\frac{\tan\beta}{\tan\alpha}}\cos 2\,p\phi\int_0^{\arctan\frac{\tan\alpha}{\cos\phi}} P_q^{2\,p}(\cos\theta)\sin\theta\,d\theta d\phi \\ &+ \int_{\frac{\pi}{2}-\arctan\frac{\tan\alpha}{\tan\beta}}^{\frac{\pi}{2}+\arctan\frac{\tan\alpha}{\tan\beta}}\cos 2\,p\phi\int_0^{\arctan\frac{\tan\beta}{(\cos\phi-\pi/2)}} P_q^{2\,p}(\cos\theta)\sin\theta\,d\theta d\phi \\ &+ \int_{\pi-\arctan\frac{\tan\beta}{\tan\alpha}}^{\pi}\cos 2\,p\phi\int_0^{\arctan\frac{\tan\alpha}{\cos(\phi-\pi)}} P_q^{2p}\,(\cos\theta)\sin\theta\,d\theta d\phi \end{aligned} \tag{12.74}$$

from which we obtain the coefficients:

$$A_{mn} = \frac{(2n+1)^2(n-2m)!\, I_{mn}}{j2\pi(n+2m)!\left(nh_{n-1}^{(2)}(kR) - (n+1)h_{n+1}^{(2)}(kR)\right)}, \tag{12.75}$$

where

$$\begin{aligned} I_{mn} = & \int_0^{\arctan\frac{\tan\beta}{\tan\alpha}} \cos 2m\phi \int_0^{\arctan\frac{\tan\alpha}{\cos\phi}} P_n^{2m}(\cos\theta)\sin\theta\, d\theta d\phi \\ & + \int_{\frac{\pi}{2}-\arctan\frac{\tan\alpha}{\tan\beta}}^{\frac{\pi}{2}+\arctan\frac{\tan\alpha}{\tan\beta}} \cos 2m\phi \int_0^{\arctan\frac{\tan\beta}{\sin\phi}} P_n^{2m}(\cos\theta)\sin\theta\, d\theta d\phi \\ & + \int_{\pi-\arctan\frac{\tan\beta}{\tan\alpha}}^{\pi} \cos 2m\phi \int_0^{\arctan\frac{\tan\alpha}{-\cos\phi}} P_n^{2m}(\cos\theta)\sin\theta\, d\theta d\phi, \end{aligned} \tag{12.76}$$

$$\begin{aligned} I_{on} = & \int_0^{\arctan\frac{\tan\beta}{\tan\alpha}} \frac{\tan\alpha}{\sqrt{\cos^2\phi + \tan^2\alpha}} P_n^{-1}\left(\frac{\cos\phi}{\sqrt{\cos^2\phi + \tan^2\alpha}}\right) d\phi \\ & + \int_{\frac{\pi}{2}-\arctan\frac{\tan\alpha}{\tan\beta}}^{\frac{\pi}{2}+\arctan\frac{\tan\alpha}{\tan\beta}} \frac{\tan\beta}{\sqrt{\sin^2\phi + \tan^2\beta}} P_n^{-1}\left(\frac{\sin\phi}{\sqrt{\sin^2\phi + \tan^2\beta}}\right) d\phi \\ & + \int_{\pi-\arctan\frac{\tan\beta}{\tan\alpha}}^{\pi} \frac{\tan\alpha}{\sqrt{\cos^2\phi + \tan^2\alpha}} P_n^{-1}\left(\frac{-\cos\phi}{\sqrt{\cos^2\phi + \tan^2\alpha}}\right) d\phi, \end{aligned} \tag{12.77}$$

and we have used the integral solutions

$$\int_0^{2\pi} \cos 2m\phi \cos 2p\phi\, d\phi = \begin{cases} \pi, & m = p \\ 0, & m \neq p \end{cases} \tag{12.78}$$

$$\int_0^{\pi} P_n^{2m}(\cos\theta) P_q^{2p}(\cos\theta)\sin\theta\, d\theta = \begin{cases} \dfrac{2(n+2m)!}{(2n+1)(n-2m)!}, & m=p \quad \text{and} \quad n=q \\ 0, & m\neq p \text{ or } n\neq q \end{cases} \tag{12.79}$$

$$\int_0^{\psi} P_n(\cos\theta)\sin\theta\, d\theta = P_n^{-1}(\cos\psi)\sin\psi \tag{12.80}$$

Far-field pressure. In the far field, we can use the asymptotic expression for the spherical Hankel function:

$$h_n^{(2)}(kr)|_{r\to\infty} = \frac{j^{n+1}}{kr} e^{-jkr}, \tag{12.81}$$

which when inserted into Eq. (12.71) gives

$$\tilde{p}(r,\theta,\phi)|_{r\to\infty} = -jk\rho_0 cS\frac{\tilde{u}_0}{4\pi r} e^{-jkr} D(\theta,\phi), \tag{12.82}$$

where S is the cap effective area given by Eq. (12.69) and

$$D(\theta,\phi) = -\frac{4\pi}{k^2 S}\sum_{n=0}^{N}\sum_{m=0}^{n/2} A_{mn} j^n P_n^{2m}(\cos\theta)\cos 2m\phi. \tag{12.83}$$

The far-field on-axis response is obtained using the relationship

$$P_n^{2m}(1) = \delta_{m0} \tag{12.84}$$

so that

$$D(0,0) = -\frac{4\pi}{k^2 S}\sum_{n=0}^{N} A_{0n} j^n. \tag{12.85}$$

The on-axis response $20\log_{10}(D(0,0))$ is plotted against kR in Fig. 12.21. The black curve shows the response of a pulsating circular cap in a sphere [from Eq. (13.83)], which has even deeper nulls than those of the oscillating cap shown in Fig. 12.18. Replacing it with a square cap, shown by the dark gray trace, immediately reduces the heights of the peaks and depths of the nulls. The smoothest response is that of the rectangular cap with an aspect ratio of 1:3 shown by the light gray trace. The worst shape is circular because at certain frequencies, the sound from near the rim arrives out of phase with that from the center and cancels it. At other frequencies it is in phase and reinforces it. By making the cap rectangular, the cancellations are never complete because the amount of sound radiated from near the corners is reduced compared with what it would be if the cap were circular.

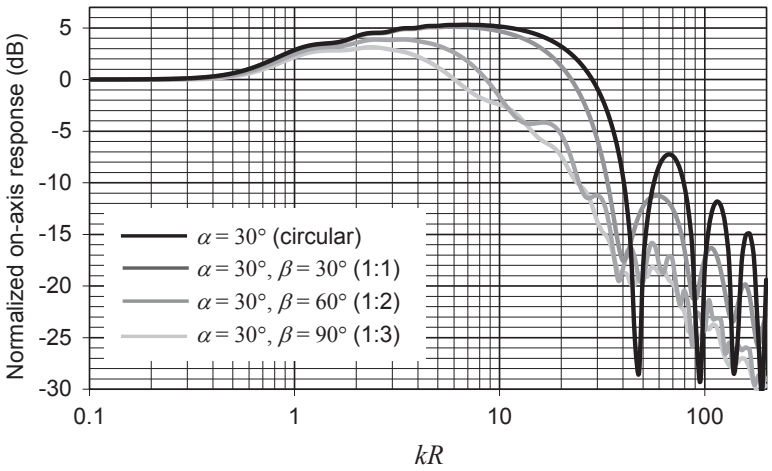

FIG. 12.21 Plot of 20 $\log_{10}(D(0,0))$ where $D(\theta,\phi)$ is the directivity function of a rectangular cap in a rigid sphere of radius R, where α and β are the two half angles of the arc formed by the cap. The axial acceleration of the cap is constant.

Frequency is plotted on a normalized scale, where $kR = 2\pi R/\lambda = 2\pi fR/c$.

Radiation impedance. The total radiation force $\tilde{F}$ is given by

$$\tilde{F} = 2R^2 \left(\int_0^{\arctan \frac{\tan\beta}{\tan\alpha}} \int_0^{\arctan \frac{\tan\alpha}{\cos\phi}} \tilde{p}(R,\theta,\phi) \sin\theta \, d\theta \, d\phi \right.$$
$$+ \int_{\frac{\pi}{2} - \arctan \frac{\tan\alpha}{\tan\beta}}^{\frac{\pi}{2} + \arctan \frac{\tan\alpha}{\tan\beta}} \int_0^{\arctan \frac{\tan\beta}{\sin\phi}} \tilde{p}(R,\theta,\phi) \sin\theta \, d\theta \, d\phi \qquad (12.86)$$
$$\left. + \int_{\pi - \arctan \frac{\tan\beta}{\tan\alpha}}^{\pi} \int_0^{\arctan \frac{\tan\beta}{-\cos\phi}} \tilde{p}(R,\theta,\phi) \sin\theta \, d\theta \, d\phi \right)$$

The specific impedance Z_s is then given by

$$Z_s = \frac{\tilde{F}}{\tilde{U}_0} = \frac{\tilde{F}}{S\tilde{u}_0} = \frac{2R^2\rho_0 c}{S} \sum_{n=0}^{\infty} \sum_{m=0}^{n/2} A_{mn} h_n^{(2)}(kR) I_{mn}, \qquad (12.87)$$

where we use the expression for S from Eq. (12.69). The real and imaginary parts, $\boldsymbol{R}_s$ and X_s, are given by

$$Z_s = \boldsymbol{R}_s + jX_s = \Re(Z_s) + j\Im(Z_s). \tag{12.88}$$

12.8 RADIATION FROM A PISTON IN A SPHERE

The geometry of the piston of radius a in a sphere of radius R is shown in Fig. 12.22. In this example we shall see the effect of having a planar radiator as opposed to the curved ones in all the previous examples. In the previous problem, the spherical cap followed the contour of the sphere so that there was only angular dependency in the velocity boundary condition with no radial dependency. This led to a direct solution for the expansion coefficients. Here a flat circular piston [4] oscillates with a uniform axial velocity of $\tilde{u}_0$. Hence the velocity boundary condition is more complicated so that the expansion coefficients can only be obtained by solving a set of simultaneous equations.

Near-field pressure. Again we assume that the pressure field generated is a general axisymmetric solution to Eq. (2.145), the Helmholtz wave equation in spherical coordinates:

$$\tilde{p}(r,\theta) = \rho_0 c\tilde{u}_0 \sum_{n=0}^{\infty} A_n h_n^{(2)}(kr)\, P_n(\cos\theta), \tag{12.89}$$

where A_n are the as-yet unknown expansion coefficients which will be calculated by means of a set of simultaneous equations in matrix form. Now we define the velocity boundary condition on the piston as

$$\tilde{u}_z(r_1,\theta) = \tilde{u}_0, \qquad 0 \le \theta \le \alpha, \qquad r = r_1, \tag{12.90}$$

where

$$r_1 = \frac{R\cos\alpha}{\cos\theta}, \tag{12.91}$$

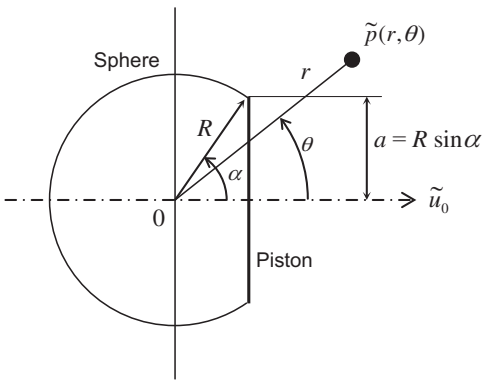

FIG. 12.22 Geometry of piston in a rigid sphere.

and the velocity boundary condition on the sphere as

$$\tilde{u}_r(R,\theta) = 0, \qquad \alpha \le \theta \le \pi, \qquad r = R, \tag{12.92}$$

where the subscript z denotes the axial direction, or normal to the piston, and the subscript r denotes the radial direction, or normal to the sphere. The piston velocity boundary condition can be obtained using

$$\tilde{u}_z(r_1,\theta) = \frac{1}{-jk\rho_0 c}\frac{\partial}{\partial z}p(r,\theta)|_{\,r=r_1}, \tag{12.93}$$

where

$$\frac{\partial}{\partial z} = \frac{\partial r}{\partial z}\cdot\frac{\partial}{\partial r} + \frac{\partial \theta}{\partial z}\cdot\frac{\partial}{\partial \theta}, \tag{12.94}$$

$$\frac{\partial r}{\partial z} = \cos\theta, \tag{12.95}$$

$$\frac{\partial \theta}{\partial z} = -\frac{\sin\theta}{r}, \tag{12.96}$$

so that

$$\tilde{u}_z(r_1,\theta) = \frac{\tilde{u}_0}{-jk}\sum_{n=0}^{\infty} A_n\left(h_n'^{(2)}(kr_1)P_n(\cos\theta)\cos\theta - \frac{1}{r_1}h_n^{(2)}(kr_1)P_n'(\cos\theta)\sin\theta\right), \tag{12.97}$$

where the derivative of the spherical Hankel function $h_n'^{(2)}(kr_1)$ is given by Eq. (12.32) and the derivative of the Legendre function $P_n{}'(\cos\theta)$ is given from Eq. (65) in Appendix II by

$$P_n{}'(\cos\theta) = \frac{\partial}{\partial\theta}P_n(\cos\theta) = -\frac{n(n+1)}{(2n+1)\sin\theta}(P_{n-1}(\cos\theta) - P_{n+1}(\cos\theta)). \tag{12.98}$$

The sphere boundary condition is the same as that for the spherical cap in a sphere given by Eq. (12.52). We also note that the area of each surface element on the piston and the sphere are given respectively by

$$\delta S_p = 2\pi\frac{r_1^2}{\cos\theta}\sin\theta\,\delta\theta, \tag{12.99}$$

$$\delta S_s = 2\pi R^2\sin\theta\,\delta\theta. \tag{12.100}$$

Hence, we can create an infinite set of simultaneous equations by multiplying Eqs. (12.90) and (12.92) through by $P_m(\cos\theta)$ and integrating over the surfaces of the piston and sphere:

$$\begin{aligned}&\int_0^{\alpha}\tilde{u}_z(r_1,\theta)P_m(\cos\theta)r_1^2\tan\theta\,d\theta + R^2\int_{\alpha}^{\pi}\tilde{u}_r(R,\theta)\,P_m\,(\cos\theta)\sin\theta\,d\theta\\ &\quad = \tilde{u}_0\int_0^{\alpha}P_m(\cos\theta)r_1^2\tan\theta\,d\theta, \qquad\qquad m = 0,1,2,\cdots.\end{aligned} \tag{12.101}$$

In matrix form this becomes

$$\mathbf{M}\cdot\mathbf{a} = \mathbf{b} \Rightarrow \mathbf{a} = \mathbf{M}^{-1}\cdot\mathbf{b}, \tag{12.102}$$

where the matrix $\mathbf{M}$ and vectors $\mathbf{a}$ and $\mathbf{b}$ are given by

$$\mathbf{M}(m+1,n+1) = \frac{I_{mn} + \left(nh_{n-1}^{(2)}(kR) - (n+1)h_{n+1}^{(2)}(kR)\right)K_{mn}}{2n+1}, \qquad \begin{cases} m = 0,1,\cdots,N \\ n = 0,1,\cdots,N \end{cases}, \tag{12.103}$$

$$\mathbf{b}(m+1) = -jL_m, \qquad m = 0,1,\cdots,N, \tag{12.104}$$

$$\mathbf{a}(n+1) = A_n, \qquad n = 0,1,\cdots,N, \tag{12.105}$$

where

$$I_{mn} = \int_0^{\alpha} \Big\{ \left(nh_{n-1}^{(2)}(kr_1) - (n+1)h_{n+1}^{(2)}(kr_1)\right)P_n(\cos\theta)\cos\theta \tag{12.106}$$

$$+n(n+1)h_n^{(2)}(kr_1)\left(P_{n-1}(\cos\theta) - P_{n+1}(\cos\theta)\right)/kr_1\Big\}P_m(\cos\theta)\frac{r_1^2}{R^2}\tan\theta\, d\theta,$$

$$K_{mn} = \int_{\alpha}^{\pi} P_n(\cos\theta)P_m(\cos\theta)\sin\theta\, d\theta, \tag{12.107}$$

$$L_m = \int_0^{\alpha} P_m(\cos\theta)\frac{r_1^2}{R^2}\tan\theta\, d\theta. \tag{12.108}$$

A solution to the integral K_{mn} is given by Eq. (70) in Appendix II. Unfortunately, integrals I_{mn} and L_m have no analytical solutions and therefore have to be evaluated numerically using, for example,

$$\int_0^{\alpha} f(\theta)\, d\theta = \frac{\alpha}{P}\sum_{p=1}^{P} f(\theta_p), \qquad \text{where } \theta_p = \frac{p-1/2}{P}\alpha. \tag{12.109}$$

Far-field pressure. In the far field, we can use the asymptotic expression for the spherical Hankel function from Eq. (12.18), which when inserted into Eq. (12.89) gives

$$\tilde{p}(r,\theta)|_{r\to\infty} = -jk\rho_0 cS\frac{\tilde{u}_0}{4\pi r}e^{-jkr}D(\theta). \tag{12.110}$$

where S is the piston area given by $S = \pi a^2$ and

$$D(\theta) = -\frac{4}{k^2R^2 \sin^2\alpha} \sum_{n=0}^{N} A_n j^n P_n(\cos\theta). \tag{12.111}$$

The directivity pattern $20 \log_{10}(D(\theta)/D(0))$ for $\alpha = 60°$ is plotted in Fig. 12.23 for various values of ka. The far-field on-axis response is given by

$$D(0) = -\frac{4}{k^2R^2 \sin^2\alpha} \sum_{n=0}^{N} A_n j^n. \tag{12.112}$$

The on-axis response $20 \log_{10}(D(0))$ is plotted against ka in Fig. 12.24. Comparing the directivity pattern of Fig. 12.23 with that of a spherical cap shown in Fig. 12.17 we see that the piston is more directional at high frequencies, concentrating its output over a decreasing angle. By contrast, the spherical cap shows a fairly constant angle of dispersion at high frequencies which is approximately equal to the angle of arc formed by the cap itself. The on-axis responses of Fig. 12.24 are quite interesting. They all show an overall 6 dB rise due to the transition from whole-space radiation at low frequencies to half-space radiation at high frequencies. In addition, there are ripples in the response above $ka = 1.5$ due to reflections from the edge of the piston, which acts as a secondary radiator interfering with the direct radiation. Furthermore, the 15° cap behaves rather like the point source on a sphere and produces ripples below $ka = 1.5$ due to diffraction around the sphere. An important difference between planar sources and curved "constant directivity" sources such as the spherical cap (see Fig. 12.18), driven with constant acceleration, is that the on-axis response of the latter rolls off in

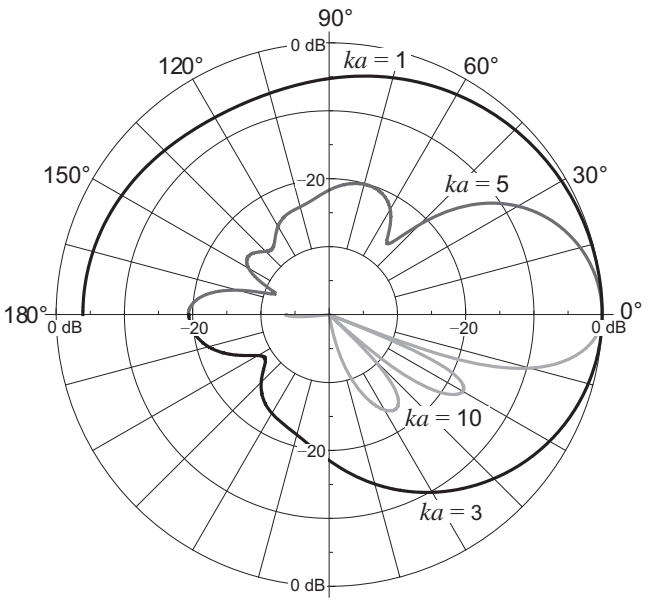

FIG. 12.23 Far field directivity pattern $20 \log_{10}(|D(\theta)|/|D(0)|)$ of the far-field pressure due to a piston of radius a in a rigid sphere for $\alpha = 60°$, where $R = a/\sin\alpha$ is the radius of the sphere.

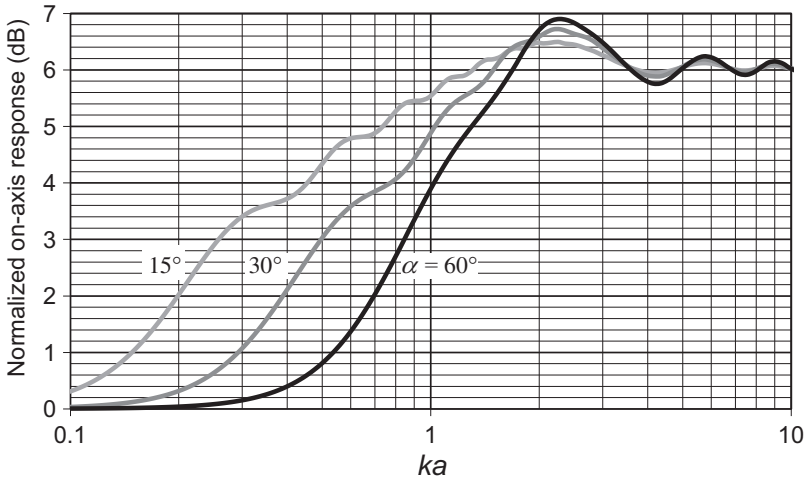

FIG. 12.24 Plot of 20 $\log_{10}(D(0))$ where $D(\theta)$ is the directivity function of a piston of radius a in a rigid sphere, where $R = a/\sin\alpha$ is the radius of the sphere. The axial acceleration of the piston is constant.

Frequency is plotted on a normalized scale, where $ka = 2\pi a/\lambda = 2\pi fa/c$.

the region where the radiation impedance is resistive and the radiated pressure is thus proportional to the velocity of the radiating surface. With a planar source, the narrowing of the directivity pattern and subsequent concentration of the radiated pressure on axis tends to compensate for this and maintain a level response. At lower frequencies, where the radiation load is mainly mass, both have a level pressure response with constant acceleration due to Newton's second law: force = mass × acceleration.

Radiation impedance. The total radiation force $\tilde{F}$ is given by

$$\tilde{F} = \int_0^{2\pi}\int_0^{\alpha} \tilde{p}(r_1,\theta) r_1^2 \tan\theta \, d\theta \, d\phi. \tag{12.113}$$

The specific impedance Z_s is then given by

$$Z_s = \frac{\tilde{F}}{\tilde{U}_0} = \frac{2\rho_0 c}{R^2 \sin^2\alpha} \sum_{n=0}^{\infty} A_n \int_0^{\alpha} h_n^{(2)}(kr_1) P_n(\cos\theta) r_1^2 \tan\theta \, d\theta, \tag{12.114}$$

where $\tilde{U}_0 = \pi R^2 \sin^2\alpha \, \tilde{u}_0$. The real and imaginary parts, $\boldsymbol{R}_s$ and X_s, are plotted in Fig. 12.25 where

$$Z_s = \boldsymbol{R}_s + jX_s = \Re(Z_s) + j\Im(Z_s). \tag{12.115}$$

The main difference between these curves and those of Fig. 12.19 for the spherical cap is that they all show ripples due to interference patterns in the immediate vicinity of the piston.

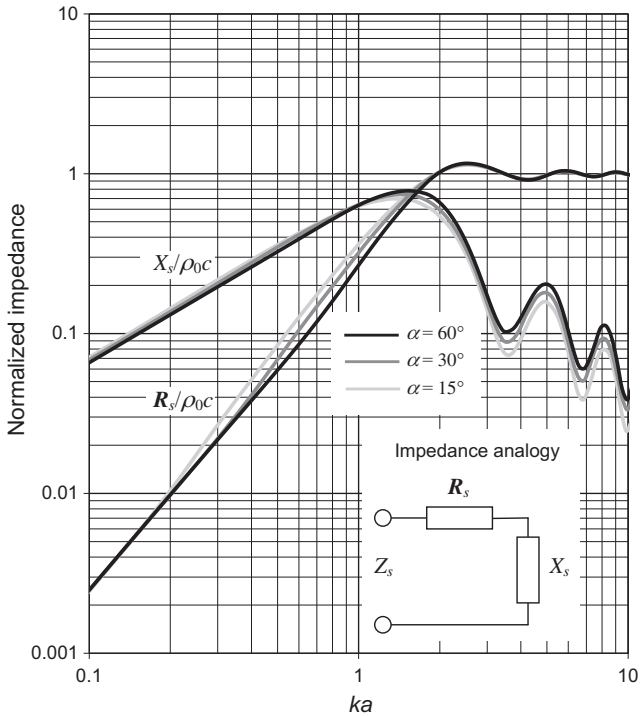

FIG. 12.25 Real and imaginary parts of the normalized specific radiation impedance $Z_s/\rho_0 c$ of the air load on an oscillating piston of radius a in a rigid sphere, where $R = a/\sin\alpha$ is the radius of the sphere.

Frequency is plotted on a normalized scale, where $ka = 2\pi a/\lambda = 2\pi fa/c$.

12.9 RADIATION FROM AN OSCILLATING CONVEX DOME IN AN INFINITE BAFFLE

A convex dome [5] of radius a and radius of curvature R in an infinite baffle is shown in Fig. 12.26. We shall solve this problem using field matching, whereby we make use of the fact that the dome in an infinite baffle produces the same field as that of two back-to-back domes in free space which oscillate in opposite directions. The latter produces a symmetrical field which is identical to that of the single dome together with its image field due to reflection from the baffle. In this way, the boundary condition of zero velocity or pressure gradient at the baffle is satisfied automatically.

Near-field pressure. Again we assume that the pressure field generated is a general axisymmetric solution to Eq. (2.145), the Helmholtz wave equation in spherical coordinates:

$$\tilde{p}(r,\theta) = \rho_0 c \tilde{u}_0 \sum_{n=0}^{\infty} A_n h_n^{(2)}(kr) P_n(\cos\theta), \tag{12.116}$$

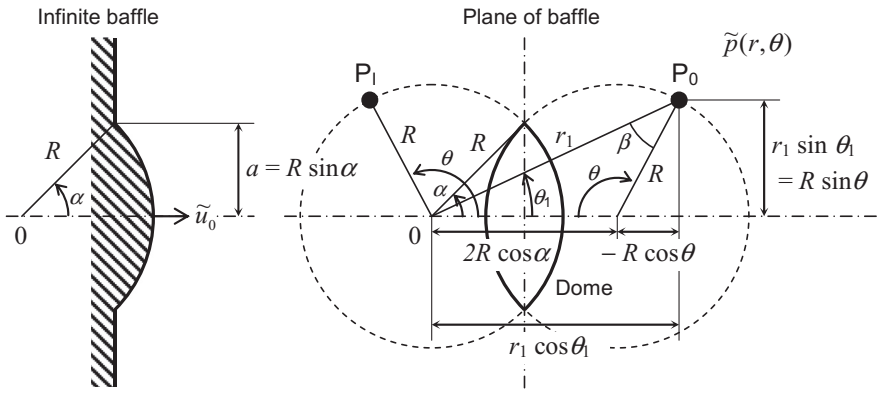

FIG. 12.26 Geometry of convex dome in infinite baffle.

where A_n are the as-yet unknown expansion coefficients which will be calculated by means of a set of simultaneous equations in matrix form. The normal particle velocity $\tilde{u}_S(R,\theta)$ at the surface of the dome is given by

$$\begin{aligned}\tilde{u}_s(R,\theta) &= \frac{1}{-jk\rho_0 c}\,\frac{\partial}{\partial r}\,p(r,\theta)|_{\,r=R} \\ &= \frac{\tilde{u}_0}{-jk}\sum_{n=0}^{\infty} A_n h_n'^{(2)}(kR)P_n(\cos\theta).\end{aligned} \tag{12.117}$$

where the derivative of the spherical Hankel function $h_n'^{(2)}(kR)$ is given by Eq. (12.32). For $\theta \le \alpha$, this is simply equal to the normal velocity of the dome. However, for $\theta > \alpha$, we are in the image field to the left of the baffle plane, as indicated by P_I in Fig. 12.26 and we need to match this velocity with that of the particle velocity $\tilde{u}_1(\theta)$ at the corresponding point P_0 to the right of the plane. The latter is defined by

$$\tilde{u}_1(r_1,\theta_1) = \frac{1}{-jk\rho_0 c}\,\frac{\partial}{\partial_n} p(r,\theta)|_{\,r=r_1,\theta=\theta_1}, \tag{12.118}$$

where the derivative is taken with respect to the normal n of the surface such that

$$\frac{\partial}{\partial n} = \frac{\partial r}{\partial n}\cdot\frac{\partial}{\partial r} + \frac{\partial\theta}{\partial n}\cdot\frac{\partial}{\partial\theta}, \tag{12.119}$$

$$\frac{\partial r}{\partial n} = \cos\beta, \tag{12.120}$$

$$\frac{\partial\theta}{\partial n} = \frac{\sin\beta}{r}. \tag{12.121}$$

The following useful relationships can be derived from the geometry of the problem:

$$\cos\beta = \frac{R}{r_1}(1 - 2\cos\alpha\cos\theta), \tag{12.122}$$

$$r_1 = R\sqrt{1 + 4\cos\alpha\,(\cos\alpha - \cos\theta)}, \tag{12.123}$$

$$\cos\theta_1 = \frac{R}{r_1}(2\cos\alpha - \cos\theta). \tag{12.124}$$

Inserting all of the above into Eq. (12.118) leads to

$$\tilde{u}_1(r_1,\theta_1) = \frac{\tilde{u}_0}{-jk}\sum_{n=0}^{\infty} A_n\left(h_n'^{(2)}(kr_1)\cos\beta P_n(\cos\theta_1) + h_n^{(2)}(kr_1)\frac{\sin\beta}{r_1}P_n'(\cos\theta_1)\right), \tag{12.125}$$

where the derivative of the spherical Hankel function $h_n'^{(2)}(kR)$ is given by Eq. (12.32) and the derivative of the Legendre function $P_n'(\cos\theta_1)$ is given by Eq. (65) from Appendix II. By matching the fields, the velocity boundary condition can be expressed by

$$\tilde{u}_s(R,\theta) = \begin{cases} \tilde{u}_0\cos\theta, & 0 \le \theta \le \alpha \\ \tilde{u}_1(r_1,\theta_1) & \alpha < \theta \le \pi. \end{cases} \tag{12.126}$$

As before, we multiply through with the orthogonal function $P_m(\cos\theta)$ and integrate over the surface of the sphere, where the area of each surface element is given by

$$\delta S = 2\pi R^2\sin\theta\,\delta\theta,$$

in order to yield the following infinite set of simultaneous equations:

$$\int_0^{\pi}\tilde{u}_s(R,\theta)P_m(\cos\theta)\sin\theta\,d\theta = \tilde{u}_0\int_0^{\alpha}P_m(\cos\theta)\cos\theta\sin\theta\,d\theta + \int_{\alpha}^{\pi}\tilde{u}_1(r_1,\theta_1)P_m(\cos\theta)\sin\theta\,d\theta, \qquad m = 0,1,2,\cdots. \tag{12.127}$$

Inserting Eqs. (12.117) and (12.125) for $\tilde{u}_s(R,\theta)$ and $\tilde{u}_1(r_1,\theta_1)$ respectively into Eq. (12.127), while truncating the infinite summation limits to order N, gives

$$\sum_{n=0}^{N} A_n\left(\frac{2\delta_{mn}\left(nh_{n-1}^{(2)}(kR) - (n+1)h_{n+1}^{(2)}(kR)\right)}{(2n+1)^2} - I_{mn}\right) = -jK_m, \qquad m = 0,1,2,\cdots,N \tag{12.128}$$

where

$$I_{mn} = \int_{\alpha}^{\pi} \left(\frac{n h_{n-1}^{(2)}(kr_1) - (n+1) h_{n+1}^{(2)}(kr_1)}{2n+1} P_n(\cos\theta_1)\cos\beta \right.$$
$$\left. - \frac{n(n+1) h_n^{(2)}(kr_1)}{(2n+1)kr_1} \left(P_{n-1}(\cos\theta_1) - P_{n+1}(\cos\theta_1)\right) \frac{\sin\beta}{\sin\theta_1} \right) P_m(\cos\theta)\sin\theta\, d\theta, \tag{12.129}$$

$$K_m = \int_0^{\alpha} P_m(\cos\theta)\cos\theta\sin\theta\, d\theta$$
$$= \begin{cases} (1-\cos^3\alpha)/3, & m = 1 \\ -\sin\alpha \dfrac{\sin\alpha\, P_m(\cos\alpha) + \cos\alpha\, P_m^1(\alpha)}{(m-1)(m+2)}, & m \neq 1, \end{cases} \tag{12.130}$$

where the identities of Eqs. (66) and (68) from Appendix II have been applied. Unfortunately, the integral I_{mn} has no analytical solution and has to be evaluated numerically using, for example:

$$\int_{\alpha}^{\pi} f(\theta) d\theta = \frac{\pi - \alpha}{P} \sum_{p=1}^{P} f(\theta_p), \qquad \text{where } \theta_p = \alpha + \frac{p - 1/2}{P}(\pi - \alpha). \tag{12.131}$$

In matrix form Eq. (12.128) becomes

$$\mathbf{M}\cdot\mathbf{a} = \mathbf{b} \Rightarrow \mathbf{a} = \mathbf{M}^{-1}\cdot\mathbf{b}, \tag{12.132}$$

where the $N\times N$ matrix elements are given by

$$\mathbf{M}(m+1, n+1) = \frac{2\delta_{mn}\left(n h_{n-1}^{(2)}(kR) - (n+1) h_{n+1}^{(2)}(kR)\right)}{j(2n+1)^2} - I_{mn}, \qquad \begin{cases} m = 0, 1, \cdots, N \\ n = 0, 1, \cdots, N \end{cases}, \tag{12.133}$$

$$\mathbf{b}(m+1) = -jK_m, \qquad m = 0, 1, \cdots, N, \tag{12.134}$$

$$\mathbf{a}(n+1) = A_n, \qquad n = 0, 1, \cdots, N, \tag{12.135}$$

Far-field pressure. In the far field, we can use the asymptotic expression for the spherical Hankel function from Eq. (12.18), which when inserted into Eq. (12.116) gives

$$\tilde{p}(r,\theta)|_{r\to\infty} = -jk\rho_0 c S \frac{\tilde{u}_0}{2\pi r} e^{-jkr} D(\theta), \tag{12.136}$$

where S is the dome effective area given by $S = \pi a^2$ and

$$D(\theta) = -\frac{2}{k^2R^2 \sin^2 \alpha} \sum_{n=0}^{N} A_n j^n P_n(\cos \theta). \tag{12.137}$$

In the case where $\alpha = ½\pi$, we obtain the following simple expansion solution from Eq. (12.60):

$$D(\theta)_{\alpha=\frac{\pi}{2}} = -j \frac{2}{k^2R^2} \sum_{n=0}^{N} \frac{(-1)^n (4n+1)^2 P_{2n}(0) P_{2n}(\cos \theta)}{(2n-1)(2n+1)\left(2nh_{2n-1}^{(2)}(kR) - (2n+1)h_{2n+1}^{(2)}(kR)\right)}. \tag{12.138}$$

The directivity pattern $20 \log_{10}(D(\theta)/D(0))$ for $\alpha = 60°$ is plotted in Fig. 12.27 for various values of ka. The results are fairly similar to those of the spherical cap in a sphere in that at low frequencies the pattern is almost omnidirectional and at high frequencies the dome cap shows a fairly constant angle of dispersion which is approximately equal to the angle of arc formed by the dome itself. The far-field on-axis response is given by

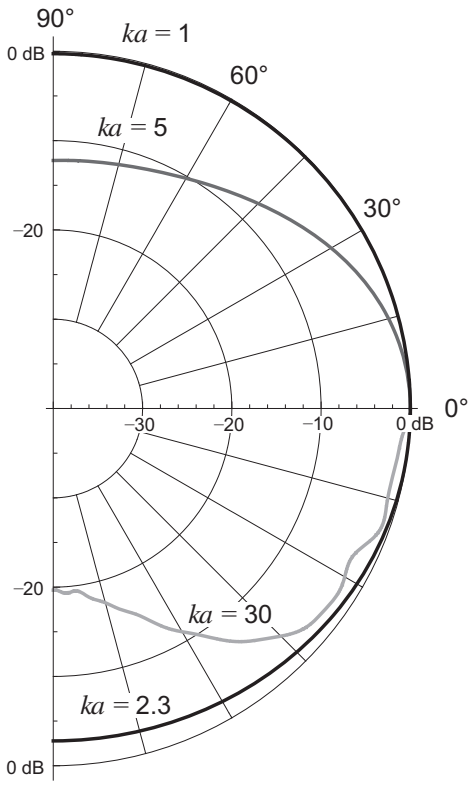

FIG. 12.27 Far-field directivity pattern $20 \log_{10}(|D(\theta)|/|D(0)|)$ of the far-field pressure due to a convex dome of radius a in an infinite baffle for $\alpha = 60°$, where α is the half-angle of the arc formed by the dome.

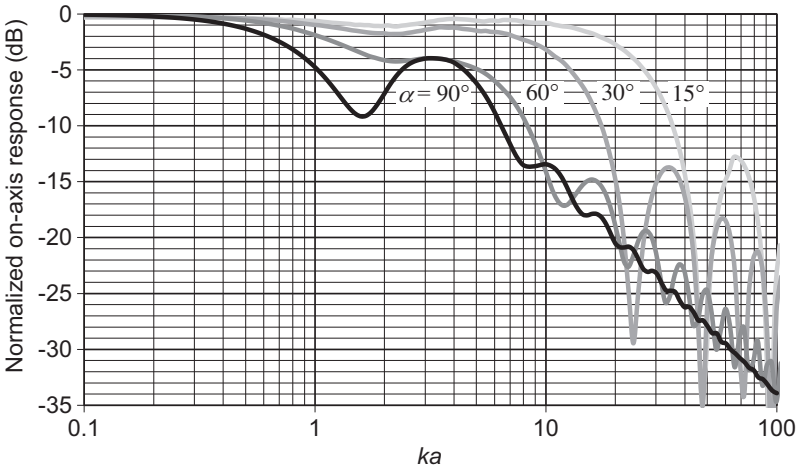

FIG. 12.28 Plot of 20 $\log_{10}(D(0))$ where $D(\theta)$ is the directivity function of a convex dome of radius a in an infinite baffle, where α is the half-angle of the arc formed by the dome. The axial acceleration of the dome is constant.

Frequency is plotted on a normalized scale, where $ka = 2\pi a/\lambda = 2\pi fa/c$.

$$D(0) = -\frac{2}{k^2R^2 \sin^2 \alpha} \sum_{n=0}^{N} A_n j^n. \tag{12.139}$$

The on-axis response $20 \log_{10}(D(0))$ is plotted against ka in Fig. 12.28. Again, the response is fairly similar to that of the spherical cap in a sphere except that there is no 6 dB level shift between low and high frequencies due to that fact that the sound is radiated into half-space at all frequencies.

Radiation impedance. The total radiation force $\tilde{F}$ is given by

$$\tilde{F} = R^2 \int_0^{2\pi} \int_0^{\alpha} \tilde{p}(R, \theta) \sin \theta \, d\theta \, d\phi, \tag{12.140}$$

using the identity of Eq. (69) from Appendix II. The specific impedance Z_s is then given by

$$Z_s = \frac{\tilde{F}}{\tilde{U}_0} = \frac{2\rho_0 c}{\sin \alpha} \sum_{n=0}^{N} A_n h_n^{(2)}(kr) P_n^{-1}(\cos \alpha), \tag{12.141}$$

where we have used the expression for $\tilde{U}_0$ from Eq. (12.49). The real and imaginary parts, $\boldsymbol{R}_s$ and X_s, are plotted in Fig. 12.29 where

$$Z_s = \boldsymbol{R}_s + jX_s = \Re(Z_s) + j\Im(Z_s). \tag{12.142}$$

Again the results are fairly similar to those for a spherical cap in a sphere except at low frequencies where the radiation impedance is greater due to the half-space radiation load.

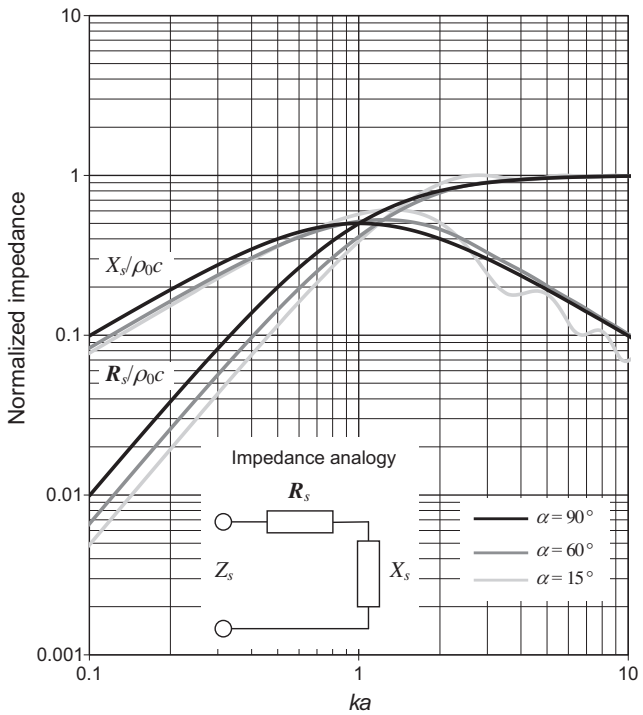

FIG. 12.29 Real and imaginary parts of the normalized specific radiation impedance $Z_s/\rho_0 c$ of the air load on a convex dome of radius a in an infinite baffle, where α is the half-angle of the arc formed by the dome.

Frequency is plotted on a normalized scale, where $ka = 2\pi a/\lambda = 2\pi fa/c$.

12.10 RADIATION FROM AN OSCILLATING CONCAVE DOME IN AN INFINITE BAFFLE

A concave dome [5] of radius a and radius of curvature R in an infinite baffle is shown in Fig. 12.30. In this problem, we shall introduce the concept of coupling whereby the field $\tilde{p}_I(r, \theta)$ inside the imaginary sphere, which includes the space inside the dome, is coupled to an external field $\tilde{p}(r, \theta)$. Again, the baffle can be removed so that we have an equivalent field which is symmetrical either side of the plane of the baffle. However, in the external field we completely ignore the dome as if it inhabited some other universe. What we have in effect is a breathing disk in free space with identical pressure distributions on both faces, which are also the same as that of the mouth of the dome. The velocity distributions are also equal in magnitude to that of the mouth, but have opposite directions. This enables us to apply the same field-matching condition as in the convex dome.

Near-field pressure. We assume that the external pressure field $\tilde{p}(r, \theta)$ in the region $r \geq R$ is a general axisymmetric solution to Eq. (2.145), the Helmholtz wave equation in spherical coordinates:

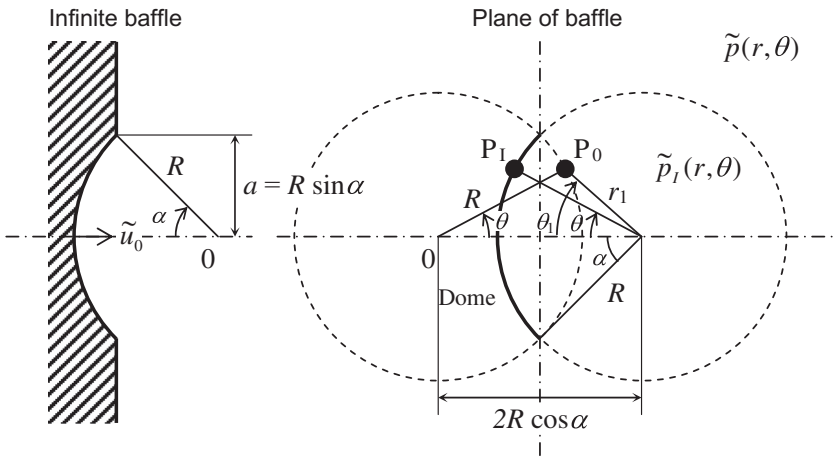

FIG. 12.30 Geometry of concave dome in infinite baffle.

$$\tilde{p}(r,\theta) = \rho_0 c\tilde{u}_0 \sum_{n=0}^{\infty} x_n h_n^{(2)}(kr)\, P_n(\cos\theta), \tag{12.143}$$

where x_n are the as-yet unknown expansion coefficients which will be calculated by means of a set of simultaneous equations in matrix form. The normal particle velocity $\tilde{u}_S(R,\theta)$ at the surface of the sphere is given by

$$\begin{aligned}\tilde{u}(R,\theta) &= \frac{1}{-jk\rho_0 c}\,\frac{\partial}{\partial r}\,p(r,\theta)|_{r=R} \\ &= \frac{\tilde{u}_0}{-jk}\sum_{n=0}^{\infty} x_n h_n'^{(2)}(kR) P_n(\cos\theta),\end{aligned} \tag{12.144}$$

where the derivative of the spherical Hankel function $h_n'^{(2)}(kR)$ is given by Eq. (12.32). The internal field $\tilde{p}_I(r,\theta)$ must be continuous everywhere in the region $r \le R$. Hence we omit the spherical Bessel function of the second kind, which has a singularity at $r = 0$, from the spherical Hankel function so that

$$\tilde{p}_l(r,\theta) = \rho_0 c\tilde{u}_0 \sum_{n=0}^{\infty} y_n j_n(kr)\, P_n(\cos\theta), \tag{12.145}$$

where y_n are the unknown expansion coefficients. The normal particle velocity $\tilde{u}_I(R,\theta)$ at the surface of the sphere is given by

$$\begin{aligned}\tilde{u}_I(R,\theta) &= \frac{1}{-jk\rho_0 c}\,\frac{\partial}{\partial r}\,p_I(r,\theta)|_{r=R} \\ &= \frac{\tilde{u}_0}{-jk}\sum_{n=0}^{\infty} y_n j_n'(kR) P_n(\cos\theta).\end{aligned} \tag{12.146}$$

At the surface of the dome, the normal particle velocity has to match the axial velocity $\tilde{u}_0$ of the dome. Hence

$$\tilde{u}_I(R,\theta) = -\tilde{u}_0 \cos\theta, \qquad 0 \le \theta \le \alpha. \tag{12.147}$$

Also, we have the coupling condition whereby the normal particle velocity on the inner surface of the imaginary sphere has to match that on its outer surface

$$\tilde{u}_I(R,\theta) = \tilde{u}(R,\theta), \qquad \alpha \le \theta \le \pi. \tag{12.148}$$

Likewise, the pressure on the inner surface of the sphere has to match that on its outer surface:

$$\tilde{p}(R,\theta) = \tilde{p}_I(R,\theta), \qquad \alpha < \theta \le \pi. \tag{12.149}$$

Finally, we apply the field matching whereby the pressure on the outer surface of the imaginary sphere is equal to that of its mirror image, which lies inside the image sphere:

$$\tilde{p}(R,\theta) = \tilde{p}_I(r_1,\theta_1), \qquad 0 < \theta \le \alpha. \tag{12.150}$$

From the geometry of the problem, we can write

$$r_1 = R\sqrt{1 + 4\cos\alpha(\cos\alpha - \cos\theta)}, \tag{12.151}$$

$$\cos\theta_1 = \frac{R}{r_1}(2\cos\alpha - \cos\theta). \tag{12.152}$$

Now we have all of the boundary conditions in place, we can create the following pair of infinite simultaneous equations in the unknown coefficients x_n and y_n in the usual manner by multiplying through by $P_m(\cos\theta)$ and integrating over the surface of the imaginary sphere together with its image and the surface of the dome:

$$\begin{aligned}\int_0^{\pi} \tilde{p}(R,\theta)P_m(\cos\theta)\sin\theta\, d\theta &= \int_0^{\alpha} \tilde{p}_I(r_1,\theta_1)\, P_m(\cos\theta)\sin\theta\, d\theta \\ &\quad + \int_{\alpha}^{\pi} \tilde{p}_I(R,\theta)P_m(\cos\theta)\sin\theta\, d\theta, \qquad m = 0,1,2,\cdots,\end{aligned} \tag{12.153}$$

$$\begin{aligned}\int_0^{\pi} \tilde{u}_I(R,\theta)P_m(\cos\theta)\sin\theta\, d\theta &= -\tilde{u}_0 \int_0^{\alpha} P_m(\cos\theta)\cos\theta\sin\theta\, d\theta \\ &\quad + \int_{\alpha}^{\pi} \tilde{u}(R,\theta)P_m(\cos\theta)\sin\theta\, d\theta, \qquad m = 0,1,2,\cdots.\end{aligned} \tag{12.154}$$

In matrix form this becomes

$$\mathbf{x} = \mathbf{A}\cdot\mathbf{y}, \tag{12.155}$$

$$\mathbf{y} = \mathbf{B}\cdot\mathbf{x} + \mathbf{c}, \tag{12.156}$$

where

$$\mathbf{x} = [x_0, x_1, \cdots x_m],\ \mathbf{y} = [y_0, y_1, \cdots y_m],$$

where the matrices $\mathbf{A}$ and $\mathbf{B}$ and vector $\mathbf{c}$ are given by

$$\mathbf{A}(m+1, n+1) = \frac{m+1/2}{h_m^{(2)}(kR)}(I_{mn} + j_n(kR)K_{mn}), \qquad \begin{cases} m = 0, 1, \cdots, N \\ n = 0, 1, \cdots, N \end{cases}, \tag{12.157}$$

$$\mathbf{B}(m+1, n+1) = \frac{m+1/2}{j'_m(kR)}h'^{(2)}_n(kR)K_{mn}, \qquad \begin{cases} m = 0, 1, \cdots, N \\ n = 0, 1, \cdots, N \end{cases}, \tag{12.158}$$

$$\mathbf{c}(m+1) = jk\frac{m+1/2}{j'_m(kR)}L_m, \qquad m = 0, 1, \cdots, N, \tag{12.159}$$

where

$$I_{mn} = \int_0^\alpha j_n(kr_1)P_n(\cos\theta_1)P_m(\cos\theta)\sin\theta\, d\theta, \tag{12.160}$$

$$\begin{aligned} K_{mn} &= \int_\alpha^\pi P_n(\cos\theta)P_m(\cos\theta)\sin\theta\, d\theta \\ &= \begin{cases} \dfrac{\sin\alpha\big(P_n(\cos\alpha)P'_m(\cos\alpha) - P_m(\cos\alpha)P'_n(\cos\alpha)\big)}{m(m+1) - n(n+1)}, & m \neq n \\ \dfrac{1 + (P_m(\cos\alpha))^2\cos\alpha + 2\displaystyle\sum_{j=1}^{m-1} P_j(\cos\alpha)(P_j(\cos\alpha)\cos\alpha - P_{j+1}(\cos\alpha))}{2m+1}, & m = n \end{cases} \end{aligned} \tag{12.161}$$

$$\begin{aligned} L_m &= \int_0^\alpha P_m(\cos\theta)\cos\theta\sin\theta\, d\theta \\ &= \begin{cases} (1 - \cos^3\alpha)/3, & m = 1 \\ -\sin\alpha\dfrac{\sin\alpha\, P_m(\cos\alpha) + \cos\alpha\, P^1_m(\cos\alpha)}{(m-1)(m+2)}, & m \neq 1, \end{cases} \end{aligned} \tag{12.162}$$

where the identities of Eqs. (66), (68), and (70) from Appendix II have been applied. Unfortunately, the integral I_{mn} has no analytical solution and has to be evaluated numerically using, for example,

$$\int_0^{\alpha} f(\theta)d\theta = \frac{\alpha}{P}\sum_{p=1}^{P} f(\theta_p), \qquad \text{where} \quad \theta_p = \frac{p-1/2}{P}\alpha. \tag{12.163}$$

Solving Eqs. (12.155) and (12.156) for $\mathbf{x}$ and $\mathbf{y}$ gives

$$\mathbf{y} = [\mathbf{I} - \mathbf{B}\cdot\mathbf{A}]^{-1}\cdot\mathbf{c}, \tag{12.164}$$

$$\mathbf{x} = \mathbf{A}\cdot\mathbf{y}. \tag{12.165}$$

Far-field pressure. In the far field, we can use the asymptotic expression for the spherical Hankel function from Eq. (12.18), which when inserted into Eq. (12.143) gives

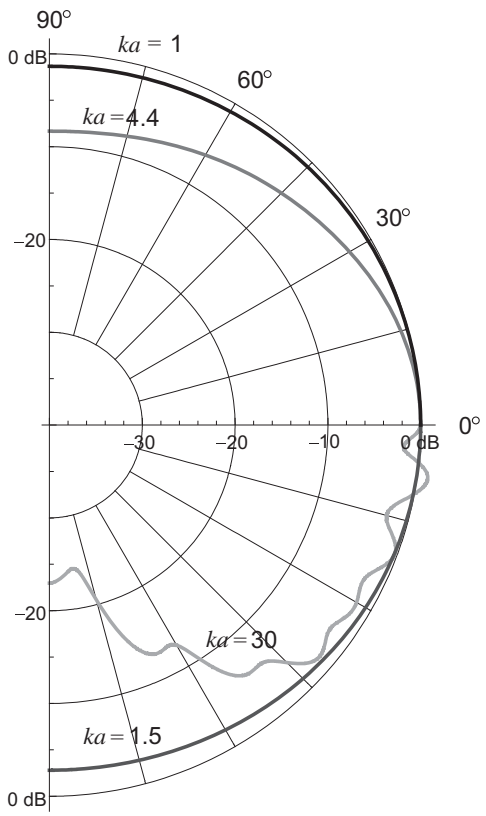

FIG. 12.31 Far field directivity pattern 20 $\log_{10}(|D(\theta)|/|D(0)|)$ of the far-field pressure due to a concave dome of radius *a* in an infinite baffle for $\alpha = 60^\circ$, where α is the half-angle of the arc formed by the dome.

$$\tilde{p}(r,\theta)\Big|_{r\to\infty} = -jk\rho_0 cS\frac{\tilde{u}_0}{2\pi r}\,e^{-jkr}\,D(\theta), \tag{12.166}$$

where S is the dome effective area given by $S = \pi a^2$ and

$$D(\theta) = -\frac{2}{k^2R^2\sin^2\alpha}\sum_{n=0}^{N} x_n j^n P_n(\cos\theta). \tag{12.167}$$

The directivity pattern $20\log_{10}(D(\theta)/D(0))$ for $\alpha = 60°$ is plotted in Fig. 12.31 for various values of ka. Not surprisingly, the directivity is similar to that of the convex dome. The far-field on-axis response is given by

$$D(0) = -\frac{2}{k^2R^2\sin^2\alpha}\sum_{n=0}^{N} x_n j^n. \tag{12.168}$$

The on-axis response $20\log_{10}(D(0))$ is plotted against ka in Fig. 12.32. This shows some interesting features. The dips in the responses of the convex dome shown in Fig. 12.28 for various values α are now replaced with resonant peaks. In each case, the resonant frequency is determined by the compliance of the dome cavity and the radiation mass. The peak is fairly broad due to the damping effect of the radiation resistance. At $ka = 4.1$ we see a sharp dip due to a radial standing wave across

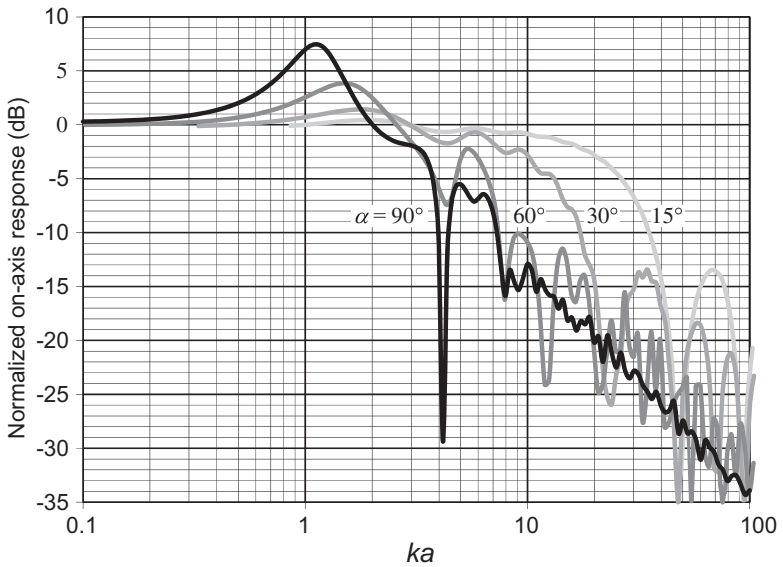

FIG. 12.32 Plot of 20 $\log_{10}(D(0))$ where $D(\theta)$ is the directivity function of a concave dome of radius a in an infinite baffle, where α is the half-angle of the arc formed by the dome. The axial acceleration of the dome is constant.

Frequency is plotted on a normalized scale, where $ka = 2\pi a/\lambda = 2\pi fa/c$.

the mouth of the dome, where the air just circulates back and forth between points of maximum and minimum pressure. Above this frequency the response is fairly uneven due to standing wave harmonics.

Radiation impedance. The total radiation force $\tilde{F}$ is given by

$$\tilde{F} = R^2 \int_0^{2\pi} \int_0^{\alpha} \tilde{p}(R, \theta) \sin \theta \, d\theta \, d\phi \tag{12.169}$$

using the identity of Eq. (69) from Appendix II. The specific impedance Z_s is then given by

$$Z_s = \frac{\tilde{F}}{\tilde{U}_0} = \frac{2\rho_0 c}{\sin \alpha} \sum_{n=0}^{N} y_n j_n(kr) P_n^{-1}(\cos \alpha), \tag{12.170}$$

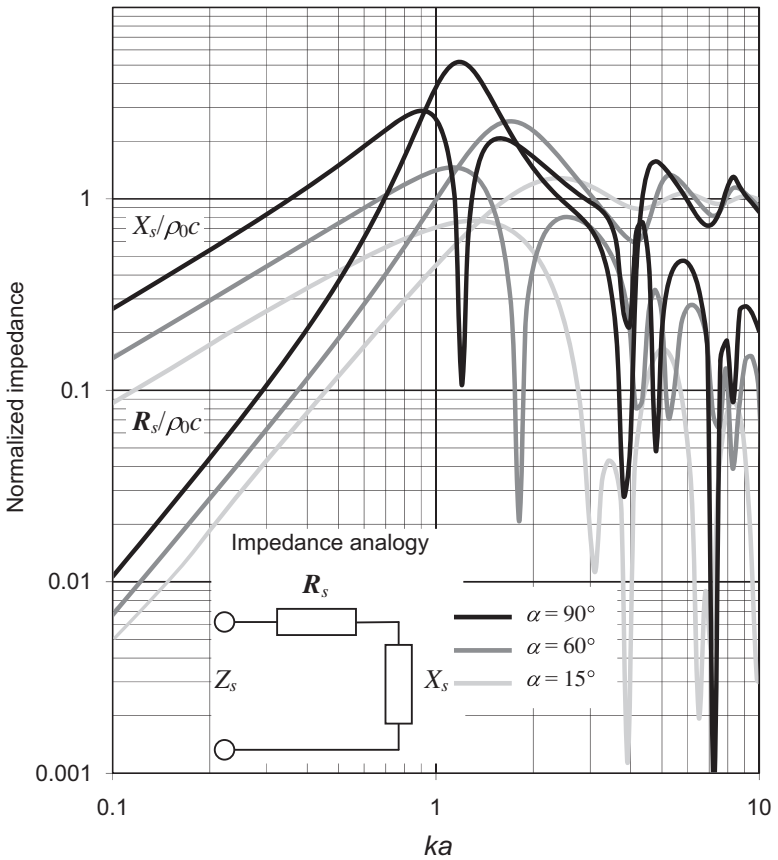

FIG. 12.33 Real and imaginary parts of the normalized specific radiation impedance $Z_s/\rho_0 c$ of the air load on a concave dome of radius *a* in an infinite baffle, where α is the half-angle of the arc formed by the dome.

Frequency is plotted on a normalized scale, where $ka = 2\pi a/\lambda = 2\pi fa/c$.

where we have used the expression for $\tilde{U}_0$ from Eq. (12.49). The real and imaginary parts, $\boldsymbol{R}_s$ and X_s, are plotted in Fig. 12.33 where

$$Z_s = \boldsymbol{R}_s + jX_s = \Re(Z_s) + j\Im(Z_s). \tag{12.171}$$

We can see from these curves that at the first peak in the radiation resistance, which more or less corresponds with the first peak in the on-axis response, the radiation reactance is at a minimum, so that the radiation efficiency is enhanced. Below this resonance, the reactance is positive due to the radiation mass. Immediately above it, the reactance is negative due to the compliance of the dome cavity. However, due to standing wave modes, the reactance is alternately positive and negative as the frequency increases above $ka = 4$.

References

[1] Stenzel H. Über die von einer starren Kugel hervorgerufene Störung des schallfeldes (On the Interference of a Sound Field Produced by a Rigid Ball). E. N. T 1938;15:71–8.

[2] Skudrzyk E. The Foundations of Acoustics: Basic Mathematics and Basic Acoustics. Wien: Springer-Verlag; 1971. pp. 396–400. Although Skudrzyk's equations are in a different form, the results agree well with those presented here.

[3] Morse PM, Ingard KU. Theoretical Acoustics. New York: McGraw-Hill; 1968:343–346.

[4] Skudrzyk E. The Foundations of Acoustics: Basic Mathematics and Basic Acoustics. Wien: Springer-Verlag; 1971. pp. 400–407. Skudrzyk's solution was obtained by a slightly different method from the one presented here and used least squares minimization whereas here it is obtained directly using the property of orthogonality. However, the two solutions show good agreement.

[5] Suzuki H, Tichy J. Sound Radiation from Convex and Concave Domes in an Infinite Baffle. J. Acoust. Soc. Am. 1981;69(1):41–9. Their solution was obtained by a slightly different method from the one presented here and used least squares minimization. However, the two solutions show good agreement.

[6] Aarts RM, Janssen AJEM. Sound radiation from a resilient spherical cap on a rigid sphere. J. Acoust. Soc. Am. 2010;127(4):2262–73.